Università degli Studi di Padova
Dipartimento di Fisica ed Astronomia "G. Galilei"

Tesi di Laurea Magistrale in Fisica

Plasmonic Nano-Hole Arrays for Quantum Efficiency Enhancement of Er^{3+} Photoemission

Laureando:
Luca Zanotto

Relatore:
Prof. Giovanni Mattei

Correlatore:
Dott.ssa Tiziana Cesca

Anno Accademico 2014/2015

Abstract

The purpose of the present thesis is the study of the interaction of plasmonic nanostructures with an emitter in close proximity. The investigation was carried out following different approaches but always with the aim of inserting the experimental results in the framework of new or existing theoretical models in order to better understand the photophysical nature of the interaction. To this aim in the framework of this thesis plasmonic nanohole arrays have been synthesised and coupled to Er-doped silica layers. The choice of Erbium as emitting source was driven by the great technological importance of this rare earth in photonics and optoelectronics, connected to the characteristic emission at 1540 nm that matches the window of minimum transmission loss for silica. For this reason the first step of the research activity was devoted to the optimization of the Er^{3+} photoluminescent properties in silica. When an emitter is placed near an interface, its optical properties will be modified. To describe this variation different contributions have to be taken into account: the variation of the local density of state due to the reflection from the interface, the coupling of the emitted radiation with propagating surface plasmons on the metal-dielectric interface and the dissipation in the overlayer. Nanostructuring the overlayer offers further opportunities for changing the optical properties of a nearby emitter. Among different plasmonic nanostructures, nanohole arrays (NHAs) can represent the ideal candidate for this purpose due to their extraordinary optical transmission (EOT): at specific frequencies determined by the hole periodicity, the light transmitted through the NHA is orders of magnitude higher than the one predicted with the classical diffraction theory. When the EOT peak was tailored with the emission wavelength of the emitter strong plasmonic coupling was demonstrated, leading to lifetime shortening with almost no dissipation in the overlayer. Finally, all the obtained results allowed the development of predictive models that can be used in the design of novel devices for different photonic applications.

Lo scopo del presente lavoro di tesi è l'analisi dell'interazione di nanostrutture plasmoniche con un emettitore. Lo studio è stato condotto seguendo diversi approcci, ma sempre con il fine di confrontare i risultati sperimentali con modelli teorici sia già noti che nuovi, in modo da comprendere appieno la natura foto-fisica dell'interazione. In questo senso nell'ambito della presente tesi sono state sintetizzati nanohole array plasmonici ed accoppiati con film sottili di silice drogata con erbio. La scelta dell'erbio come emettitore è stata dettata dalla sua grande importanza tecnologica nella fotonica e nell'optoelettronica, associata alla caratteristica emissione radiativa a 1540 nm, che si trova nella finestra di minimo assorbimento ottico della silice. Per questa ragione il primo passo dell'attività di ricerca è stato volto all'ottimizzazione delle proprietà di fotoluminescenza dello ione erbio in silice. Quando un emettitore è posto in prossimità di un film sottile le sue proprietà ottiche vengono modificate. Per descrivere tale variazione è necessario tenere conto di contributi differenti: la variazione della densit locale degli stati dovuta alla riflessione all'interfaccia, l'accoppiamento della radiazione emessa con plasmoni di superficie propaganti sull'interfaccia metallo-dielettrico e infine la dissipazione nel film. La nanostrutturazione del film può offrire ulteriori opportunit nella modifica delle propriet ottiche di un emettitore. Tra le diverse nanostrutture plasmoniche, i nanohole arrays (NHAs) possono essere visti come i candidati ideali per questo scopo grazie alla loro trasmissione ottica straordinaria (EOT): a determinate lunghezze d'onda definite dalla periodicit dei buchi e dalle proprietà dielettriche dei materiali coinvolti, la luce trasmessa attraverso il NHA è ordini di grandezza più grande rispetto a quella predetta dalla teoria classica della diffrazione. Quando il picco della EOT è risonante con la lunghezza d'onda di emissione dell'emettitore, è stato dimostrato un forte accoppiamento plasmonico che porta ad un marcato accorciamento del tempo di vita nella quasi assenza di dissipazione nella nanostruttura. Infine, tutti questi risultati hanno permesso lo sviluppo di modelli predittivi che possono essere utilizzati nella progettazione di nuovi dispositivi per diverse applicazioni fotoniche.

Contents

Introduction

The interest in the so called nanoscale materials has been gaining great importance in the scientific community during the last decades, due to the discover of new properties arising as the size of a system ranges between few and hundreds of nanometres. These peculiar features are not present in materials with macroscopic size, but also disappear at the atomic scale. In particular, a lot of morphological and chemical characteristics, that are intrinsic at the macroscopic scale, become dependent on the size, shape and dielectric environment.

The first acknowledgement of the importance of the nanoscale is attributed to Richard Feynman, in his lecture "There is plenty of room at the bottom" [1], where he first suggested that the properties of materials and devices at nanometre range would present future opportunities.

The meaning of the term *Nanotechnology* could be explained with the words of N. Taniguchi [2], the first to use this term in 1974: *Nanotechnology mainly consists of the processing of separation, consolidation, and deformation of materials by one atom or by one molecule.* Since then a lot of techniques for processing materials in the way described by Taniguchi have been developed and produced important innovations in many fields, as biological sensors, surface coating, catalysis, computer science, optics, and many others.

One of the most fascinating fields in nanoscience is the study of the interaction of light with metallic nanostructures, since it exhibits unique properties absent in the macro-world. The study of the optical properties of radiation at the nanoscale, goes under the name of nanophotonics. In particular the branch that handles with the interaction between the interfaces of nanostructured metals (in particular noble metals) and electromagnetic radiation, is named *Plasmonics*. The purpose of the research in this field is to have a control on the confinement of light over distances smaller than the wavelength and over the consequent enhancement of the optical near-field [3].

Among the various possible applicative scopes of plasmonics, the one on which this thesis work focuses, is the interaction between an emitter of electromagnetic radiation and a plasmonic nanostructure placed in close proximity. This configuration allows the interface to modify the decay rate of the emitter, thanks to the coupling in the near-field with *Surface Plasmon Polaritons (SPPs)*, i.e. propagating electromagnetic waves confined at the surface of a metal [3].

In principle the excitation of SPPs is not allowed on a flat interface due to a mismatch between the momentum of impinging radiation and the propagation constant of the SPP, but thanks to the wide range of wave-vectors available in close proximity ($d \ll \lambda_{em}$) of a dipole-like emitter, the coupling with SPPs in near-field becomes possible and this increases the de-excitation probability.

Moreover, once obtained the excitation of surface modes, they could re-excite the emitter or at least couple out into far-field radiation if a grating that matches the momentum is present. This grating properties can be achieved nanostructuring the metal interface in an ordered way with the periodical properties of a lattice. This allows to obtain the necessary coupling and thus to get

an increased efficiency of the photo-emission.

This work focuses on the study of the optical properties of so-called *nanohole arrays*, i.e. ordered lattices of nanometric holes on a thin film of a noble metal. As first observed by Ebbesen et al. in 1998 [4] the characteristic feature of these structures is to give rise to an *extraordinary optical transmission (EOT)* at a particular resonant wavelength, i.e. the transmitted intensity of from the holes is much higher than the intensity impinging on the total holes' area. The position of the resonance can be chosen by varying the lattice parameter of the nanohole array.

There are multiple possible applications of nanohole arrays, most of them not yet investigated. This study is focused on the possible application of ordered arrays of holes in the coupling with the emitted radiation from erbium ions (Er^{3+}) embedded in a silica matrix. If the ions are placed in close proximity of a metal interface, the local photonic density of state is modified [5] and this produces a variation in the radiative lifetime of the state of the emitter, thanks to the near-field coupling with SPPs. Moreover the grating properties of the lattice of holes permits to couple-out the SPPs to the far-field.

The choice of the erbium as the emitter is related to its technological importance connected to the characteristic emission at 1540 nm, that matches the window of minimum transmission loss for silica. Erbium doped fiber amplifiers are in fact widely used to compensate losses in the transmission of optical signals over long distances. However, the Er-doped glass technological applications are limited by the small excitation cross-section and the long lifetime of the Er excited state [6]. Thus finding a way to enhance the efficiency of the emission can lead to important improvement in the optical communication field.

The work is divided in two main parts: the first concerns the theoretical description of the plasmonic properties, the fabrication and characterization of nanohole arrays (**sec. 1, 2, 3**), and the second on the optical features of erbium and the study of the influence of nanohole arrays on the efficiency of its photo-emission properties (**sec. 4, 5, 6**).

1 Interaction between metallic nano-structures and electromagnetic radiation

1.1 Electronic properties of metals

The interaction of metals with electromagnetic fields can be understood in a classical framework based on Maxwell's equations. Following [3] it's shown that even metallic nano-structures down to the order of a few nanometres can be described without a need to resort to quantum mechanics, since high density of free carriers results in minute spacings of the electron energy levels, compared to thermal excitation.

Thanks to the strong dependence of the optical properties on frequency, a great variety of optical phenomena occurs in metals. For low frequencies, up to far-infra-red, metals are highly reflective and do not allow electromagnetic waves to propagate through them. In this regime the *perfect conductor approximation* of infinite or fixed finite conductivity is often valid, since only negligible part of the radiation penetrates into the metal. As frequency rises towards near-infra-red and visible part of the spectrum, field penetration increases significantly, leading to considerable dissipation, and make it difficult to scale the behaviour of the metal from the low frequency regime. Finally, at ultraviolet frequencies, metals acquire dielectric character and allow the propagation of electromagnetic radiation, with refractive index and absorption depending on electronic structure. Alkali metals exhibit an almost free-electron-like response and become transparent to UV radiation, noble metals instead, show a strong absorption in UV range, caused by inter-band transitions.

The fundamental quantity to describe optical and dispersive properties, in a classical way, is the *complex dielectic function* $\epsilon(\omega)$, which can be calculated theoretically and measured experimentally.

The start of the study of electromagnetic response of metals are the macroscopic Maxwell's equations:

$$\nabla \cdot \mathbf{D} = \rho_{ext} \tag{1.1}$$

$$\nabla \cdot \mathbf{B} = 0 \tag{1.2}$$

$$\nabla \times \mathbf{E} = -\frac{\partial \mathbf{B}}{\partial t} \tag{1.3}$$

$$\nabla \times \mathbf{H} = \mathbf{J_{ext}} + \frac{\partial \mathbf{D}}{\partial t} \tag{1.4}$$

These equations link the macroscopic fields, electric $\mathbf{E}$, magnetic $\mathbf{B}$, dielectric displacement $\mathbf{D}$ and magnetic induction $\mathbf{H}$, with the external charge density ρ_{ext} and the external current density $\mathbf{J_{ext}}$. Clearly there are internal current and charge density too, so that in total $\rho_{tot} = \rho_{ext} + \rho$ and $\mathbf{J_{tot}} = \mathbf{J_{ext}} + \mathbf{J}$. Constitutive equations lead to introduce two more fields, polarization $\mathbf{P}$ and

magnetization $\mathbf{M}$, connected to the others via:

$$\mathbf{D} = \epsilon_0 \mathbf{E} + \mathbf{P} \tag{1.5}$$

$$\mathbf{H} = \frac{1}{\mu_0}\mathbf{B} - \mathbf{M} \tag{1.6}$$

Magnetic response represented by $\mathbf{M}$ is not considered for purely plasmonic systems, since only non-magnetic media are treated. Polarization $\mathbf{P}$ describes the electric dipole moment per unit volume and it's related to the internal charge density via $\nabla \cdot \mathbf{P} = -\rho$. Charge conservation ($\nabla \cdot \mathbf{J} = -\frac{\partial \rho}{\partial t}$) imposes that:

$$\mathbf{J} = \frac{\partial \mathbf{P}}{\partial t} \tag{1.7}$$

With this approach the macroscopic electric field includes all polarization effects.

Now if the medium is linear, isotropic and non-magnetic, $\mathbf{D}$ and $\mathbf{H}$ are proportional to $\mathbf{E}$ and $\mathbf{B}$, and the relations between them can be expressed using relative permittivity ϵ and magnetic permeability μ:

$$\mathbf{D} = \epsilon_0 \epsilon \mathbf{E} \tag{1.8}$$

$$\mathbf{B} = \mu_0 \mu \mathbf{H} \tag{1.9}$$

The last constitutive relationship needed is:

$$\mathbf{J} = \sigma \mathbf{E} \tag{1.10}$$

where σ is the conductivity.

Equations (1.8) and (1.10) are correct only for linear medium, without spatial and temporal dispersion, but for metal, whose properties depend on frequency, the non-locality in space and time is to br taken into account , generalizing the linear relationships:

$$\mathbf{D}(\mathbf{r}, t) = \epsilon_0 \int dt' \mathbf{dr'} \epsilon(\mathbf{r - r', t - t'}) \mathbf{E}(\mathbf{r', t'}) \tag{1.11}$$

$$\mathbf{J}(\mathbf{r}, t) = \int dt' \mathbf{dr'} \sigma(\mathbf{r - r', t - t'}) \mathbf{E}(r', t') \tag{1.12}$$

Taking the Fourier Transform of (1.11), the fields are decomposed into individual plane-wave components of wave vector $\mathbf{K}$ and angular frequency ω, obtaining:

$$\mathbf{D}(\mathbf{K}, \omega) = \epsilon_0 \epsilon(\mathbf{K}, \omega) \mathbf{E}(\mathbf{K}, \omega) \tag{1.13}$$

$$\mathbf{J}(\mathbf{K}, \omega) = \sigma(\mathbf{K}, \omega) \mathbf{E}(\mathbf{K}, \omega) \tag{1.14}$$

After these considerations the relation between conductivity and relative permittivity (from now on called the *dielectric function*) can be written:

$$\epsilon(\mathbf{K}, \omega) = 1 + \frac{i\sigma(\mathbf{K}, \omega)}{\epsilon_0 \omega} \tag{1.15}$$

Due to this intimate relationship either quantity can be used to describe electromagnetic phenomena. Historically at optical frequencies is preferable to use the dielectric function $\epsilon(\mathbf{K}, \omega)$, and since this work investigates properties in NIR-Vis range, so only dielectric function will be considered.

While studying the interaction of light with metals, a simplification in the limit of a spatially local response can be introduced. This is valid as long as the wavelength λ of the EM radiation in the material is significantly larger than all typical dimensions of the medium, such the unit cell size and mean free path of electrons. This condition is fulfilled up to UV frequencies ($\lambda \lesssim 100nm$). Under this assumption $\epsilon(\mathbf{K} = \mathbf{0}, \omega) = \epsilon(\omega)$.

In general ϵ is a complex valued function, depending on the angular frequency ω, which is real: $\epsilon(\omega) = \epsilon_1(\omega) + i\epsilon_2(\omega)$ can be written. Experimentally ϵ can be determinate via reflectivity measurements, thanks to the relation with the complex refractive index $\tilde{n} = n(\omega) + ik(\omega)$:

$$\tilde{n} = \sqrt{\epsilon}. \tag{1.16}$$

The imaginary part of the refractive index $k = \frac{\epsilon_2}{2n}$, is called the *extinction coefficient* and determines the optical absorption of EM radiation propagating through a medium. It's proportional to the absorption coefficient α of the Beer's law of attenuation in a medium ($I(x) = I_0 e^{-\alpha x}$) by the relation:

$$\alpha(x) = \frac{2k(\omega)\omega}{c} \tag{1.17}$$

Therefore, the imaginary part ϵ_2 of the dielectric function determines the amount of absorption. For $|\epsilon_1| \gg |\epsilon_2|$, the real part n of the refractive index, quantifying the lowering of the phase velocity of the propagating waves due to the polarization of the material, is mainly determined by ϵ_1.

It's useful to look for travelling-wave solutions of Maxwell's equations in absence of external stimuli. Combining the curl equations (1.1) yields the *wave equation*:

$$\nabla \times \nabla \times \mathbf{E} = -\mu_0 \frac{\partial^2 \mathbf{D}}{\partial t^2} \tag{1.18}$$

$$\mathbf{K}(\mathbf{K} \cdot \mathbf{E}) - K^2 \mathbf{E} = -\epsilon(\mathbf{K}, \omega) \frac{\omega^2}{c^2} \mathbf{E} \tag{1.19}$$

in the time and Fourier domains, respectively. Two cases need to distinguished, depending on the polarization direction of the electric field vector. For transverse waves, $\mathbf{K} \cdot \mathbf{E} = 0$, leading to the generic dispersion relation:

$$K^2 = \epsilon(\mathbf{K}, \omega) \frac{\omega^2}{c^2} \tag{1.20}$$

For longitudinal waves, we obtain:

$$\epsilon(\mathbf{K}, \omega) = 0 \tag{1.21}$$

signifying that the longitudinal collective oscillations can occur at frequencies corresponding to zeros of $\epsilon(\omega)$.

1.1.1 Drude Model

As pointed out before, the dielectric function $\epsilon(\omega)$ describes most of the information about the interaction between metals and EM radiation. In a large frequency range, including NIR and VIS, the simple Drude model of free electron gas permits to calculate the dielectric function. This a *plasma mode* in which an electron gas of density n is supposed to move against a fixed lattice of positive ions. It's to note that this approach has limited validity for noble metals, because of inter-band transitions, that occur at visible frequencies: this kind of transitions need more sophisticated model, treated in section 1.1.2. In this model electrons are supposed to be free particles, neglecting details of lattice potential and electron-electron interactions, the only assumption is that some features of the band structure are incorporated into the effective optical mass m of the electron.

If an EM radiation is applied to the metal, electrons oscillate according to the external field, and their motion is damped via collisions against the ions, with a collision frequency $\gamma = \frac{1}{\tau}$. At room temperature the relaxation time τ of the free electron gas is typically $\approx 10^{-14}s$, and the frequency $\approx 100MHz$.

Considering a free electron and a driving electric field $\mathbf{E}$ a simple equation of motion is obtained:

$$m\ddot{\mathbf{x}} + m\gamma\dot{\mathbf{x}} = -e\mathbf{E} \tag{1.22}$$

Assuming a time harmonic time dependence for the external electric field, $\mathbf{E}(t) = \mathbf{E_0}e^{-i\omega t}$, the steady state solution has the same harmonic dependence $\mathbf{x}(t) = \mathbf{x_0}e^{-i\omega t}$, where $\mathbf{x}_0$ is a complex value, which incorporates any phase shift between driving field and response via:

$$\mathbf{x}(t) = \frac{e}{m(\omega^2 + i\gamma\omega)}\mathbf{E}(t) \tag{1.23}$$

Being $\mathbf{x}(t)$ single electron displacement, the electric dipole moment $\mathbf{p}(t) = -e\mathbf{x}(t)$ can be written. Combining the effect of all n electrons in a unit volume, macroscopic polarization P writes:

$$\mathbf{P} = -ne\mathbf{x} = -\frac{ne^2}{m(\omega^2 + i\gamma\omega)}\mathbf{E} \tag{1.24}$$

Inserting this in (1.5) the displacement $\mathbf{D}$ results:

$$\mathbf{D} = \epsilon_0(1 - \frac{\omega_p^2}{\omega^2 + i\gamma\omega})\mathbf{E} \tag{1.25}$$

where the *plasma frequency* of the gas $\omega_p^2 = \frac{ne^2}{\epsilon_0 m}$ was introduced. From this the dielectric function of the Drude model is obtained:

$$\epsilon(\omega) = 1 - \frac{\omega_p^2}{\omega^2 + i\gamma\omega} = (1 - \frac{\omega_p^2}{\omega^2 + \gamma^2}) + i(\frac{\omega_p^2\gamma}{\omega(\omega^2 + \gamma^2)}) = \epsilon_1(\omega) + i\epsilon_2(\omega) \quad (1.26)$$

Different regimes can now be distinguished by varying ω compared to ω_p. The model gives good results for $\omega < \omega_p$, but fails in the regime of high frequencies $\omega \gg \omega_p$, where $\epsilon(\omega) \to 1$ is expected. In fact real metals and in particular noble metals (like Au, Ag, Cu), important in plasmonics, have the filled d band close to the Fermi surface, and this produce a high polarization. Taking into account this additional polarization of the ion cores by adding a term $\mathbf{P}_\infty = \epsilon_0(\epsilon_\infty - 1)\mathbf{E}$ to (1.5), where $\mathbf{P}$ now represent the polarization due to free electrons only. With this correction dielectric function becomes:

$$\epsilon(\omega) = (\epsilon_\infty - \frac{\omega_p^2}{\omega^2 + \gamma^2}) + i(\frac{\omega_p^2\gamma}{\omega(\omega^2 + \gamma^2)}) \quad (1.27)$$

where $\epsilon_\infty \simeq 1 \div 10$. Validity of this free electron approach is shown in 1 where experimental data from Johnson and Christy [7] are compared to the dielectric function of Drude model. Model agrees with experimental measurements as long as inter-band transitions are negligible, in particular for copper and gold below $2eV$ $(600nm)$ and for silver below $4eV$ $(300nm)$. The occurrence of inter-band transition above this energies leads to an increase of absorption, linked to ϵ_2.

Clearly an advantage of having analytical formula for dielectric function is that it can be easily included in numerical solvers for Maxwell's equations.

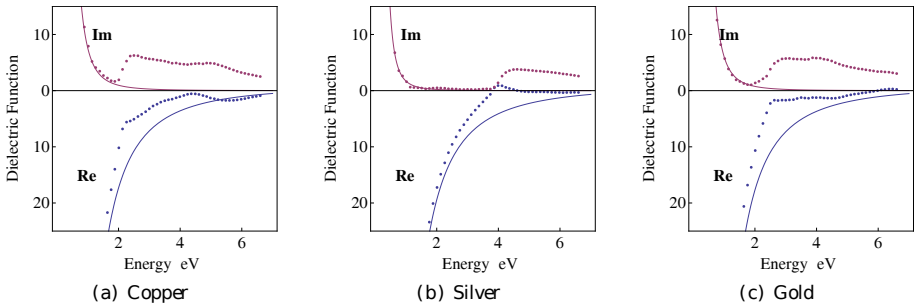

Figure 1: Solid line represents dielectric function $\epsilon(\omega)$ from Drude model fitted to experimental data from Johnson and Christy [7] (dotted line)

1.1.2 Lorentz-Drude model

It has been pointed out that for noble metals the Drude model is not adequate for describing the dielectric function at high frequencies. Above the band edge thresholds, incident radiation is efficient in inducing inter-band transitions in the bounded d electrons, below the Fermi surface, to higher bands, yielding absorption and competition between excitations of s and d electrons.

	$Au(\epsilon_\infty = 1.1156, \sigma/\epsilon_0 = 1355.01 s^{-1})$			$Ag(\epsilon_\infty = 1.4783, \sigma/\epsilon_0 = 3157.56 s^{-1})$		
	A_i[eV]	B_i[eV^2]	C_i[eV^2]	A_i[eV]	B_i[eV^2]	C_i[eV^2]
$i=1$	$-8.577 \cdot 10^4$	$-1.156 \cdot 10^4$	$5.557 \cdot 10^7$	$-1.160 \cdot 10^5$	-3050	$3.634 \cdot 10^8$
$i=2$	-2.875	0.0	$2.079 \cdot 10^3$	-4.252	-0.8385	112.2
$i=3$	-997.6	-3090	$6.921 \cdot 10^5$	-0.4960	-13.85	1.815
$i=4$	-1.630	-4.409	26.15	-2.118	-10.23	14.31

Table 1: Coefficients of L4 model for Au and Ag

The model inadequacy can be overcome by adding a term in the equation of motion (1.22):

$$m\ddot{\mathbf{x}} + m\gamma\dot{\mathbf{x}} + m\omega_0^2\mathbf{x} = -e\mathbf{E} \tag{1.28}$$

Inter-band transitions are included considering the bounded electrons as oscillators with resonance frequency ω_0. This frequency corresponds to a certain inter-band transition with $\hbar\omega_0$ energy. If other inter-band transitions are considered, there will be the same number of equations like (1.28) to solve. Each of this equations leads to a Lorentz-oscillator term of the form:

$$\frac{A_i}{\omega_i^2 - \omega^2 - i\gamma_i\omega} \tag{1.29}$$

to add up to the dielectric function yet calculated for free-electrons. Here ω is the radiation frequency, while ω_i is the resonance frequency of the i-th inter-band transition [8]. If N inter-band transitions are considered, the dielectric function results:

$$\epsilon(\omega) = \epsilon_\infty - \frac{\omega_p^2}{\omega^2 + i\gamma\omega} + \sum_{i=1}^{N} \frac{A_i}{\omega_i^2 - \omega^2 - i\gamma_i\omega} \tag{1.30}$$

Reminding the relationship between ϵ and σ and renaming coefficients, dielectric function becomes:

$$\epsilon(\omega) = \epsilon_\infty - \frac{i\sigma}{\epsilon_0\omega} + \sum_{i=1}^{N} \frac{C_i}{\omega^2 + iA_i\omega + B_i} \tag{1.31}$$

Coefficients were calculated by Nordlander and Hao [9] taking account of four transitions (*L4* model) and are shown in 1. It appears from 2 that analytical dielectric function fits very well experimental data, and it become helpful for numerical calculations.

1.2 Plasmon polaritons

1.2.1 Volume plasmons

When considering the high frequency regime ($\omega > \omega_p \gg \gamma$, neglecting interband contribution) for the ϵ of the Drude model, metals are transparent to the radiation. Therefore $\epsilon(\omega)$ is predominantly real and the imaginary part can be neglected, so it results:

$$\epsilon(\omega) \sim \epsilon_1(\omega) = 1 - \frac{\omega_p^2}{\omega^2} \tag{1.32}$$

Combining this dielectric function with Maxwell's equations (1.1), assuming $\mathbf{J_{ext}} = 0$, a wave equation is obtained, supporting propagating waves whose dispersion relation is:

$$\omega^2 = \omega_p^2 + K^2 c^2 \tag{1.33}$$

For $\omega < \omega_p$ the propagation of transverse electromagnetic waves is forbidden, instead for $\omega > \omega_p$, the plasma supports transverse waves propagating with group velocity $v_g = \frac{d\omega}{dK} < c$. The significance of the plasma frequency ω_p can be clarified, recognizing that in the small damping limit, $\epsilon(\omega_p) = 0$ (for $\mathbf{K} = 0$), which corresponds to a collective longitudinal mode. The physical significance of the excitation at ω_p can be understood considering the collective longitudinal oscillation of the conduction electron gas versus the fixed positive background of the ions cores, in the long-wavelength limit. The quanta of this oscillations are called *volume plasmons*, due to their longitudinal nature, they do not couple with transverse EM waves and can only be excited by particle impact.

1.2.2 Surface plasmon polaritons

Another kind of electromagnetic excitations, the one relevant in this work and for photonic applications of metals, are *Surface plasmons (SP)*. This type of plasmons are excitations propagating at the interface between a dielectric and

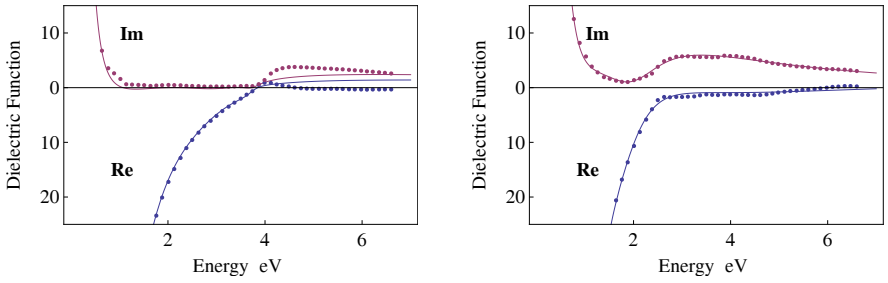

(a) Silver (b) Gold

Figure 2: Dielectric constant from *L4* model and experimental data from Johnson and Christy [7].

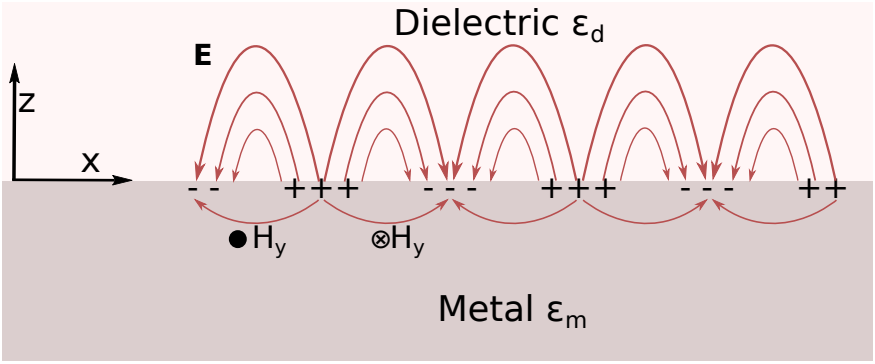

Figure 3: Geometry for SPP propagation at interface berween a metal and a dielectric. Electric and magnetic fields for the p-polarized SPP are also described.

a conductor, and their peculiarity is the ability to confine electromagnetic fields at length scales smaller than the wavelength. If the interface is extended they are called *Surface plasmon polaritons (SPP)*, if it's related to three-dimensional nanoparticles, they are named *Localized surface plasmons (LSP)*.

The coupling of light with SPPs can be described starting from the wave equation:

$$\nabla^2\mathbf{E} - \frac{\epsilon}{c^2}\frac{\partial^2\mathbf{E}}{\partial t^2} = 0 \tag{1.34}$$

with the assumption that the variation of ϵ is negligible over distances on the order of one optical wavelength. This is solved assuming a harmonic dependence of the field $\mathbf{E}$, $\mathbf{E}(\mathbf{r},t) = \mathbf{E}(\mathbf{r})e^{-i\omega t}$, obtaining the *Helmholtz equation*:

$$\nabla^2\mathbf{E} + k_0^2\epsilon\mathbf{E} = 0 \tag{1.35}$$

with $k_0 = \frac{\omega}{c}$, the wave vector of the radiation propagating in vacuum.

Assuming a semi-infinite plane interface that coincides with $z = 0$, waves travel along x-axis and ϵ depends only on z-direction. In this geometry propagating waves at $z = 0$ can be described as $\mathbf{E}(x,y,z) = \mathbf{E}(z)e^{i\beta x}$, where β, the *propagation constant*, is the component of the wave vector along the direction of propagation.

This leads to a simplified form of (1.35):

$$\frac{\partial^2\mathbf{E}(z)}{\partial z^2} + (k_0^2 - \beta^2)\mathbf{E}(z) = 0 \tag{1.36}$$

and a similar equation for magnetic field $\mathbf{H}$ is found.

Now imposing the correct boundary conditions on fields, two sets of solutions for (1.36) are obtained:

- *Transverse magnetic* (TM), in which only the field components E_x, E_z, H_z are non-zero

- *Transverse electric* (TE), where only H_x, H_z, E_y being non-zero

Once defined the scattering plane, where incident and reflected wave-vectors lay, TM has the magnetic field perpendicular to this plane, TE the electric one.

Now if the considered single flat interface is between a dielectric, non absorbing medium ($z > 0$) with positive, real dielectric constant ϵ_d and an adjacent conducing half space ($z < 0$) described by a dielectric function $\epsilon_m(\omega)$, with the requirement of metallic character, $Re[\epsilon_m(\omega)] < 0$ and solutions required are confined to the interface, i.e. with exponential decay in perpendicular z-direction, only TM modes are allowed, finding the dispersion relation:

$$\beta = \sqrt{\frac{\epsilon_m \epsilon_d}{\epsilon_m + \epsilon_d}} \tag{1.37}$$

where ϵ_m and ϵ_d are the dielectric functions of the metal and the dielectric.

Now this relation can be studied in two cases, for metals with or without attenuation:

Ideal conductor If the metal has no attenuation i.e., it has purely real dielectric function, an explicit dispersion relation can be found. In figure 4 real and imaginary parts of the dispersion relation $\omega(\beta)$ are plotted, and it's clear that SPP excitations correspond to the part of the dispersion curve which lies on the right of the light lines. In the limit of small wave vectors (IR or lower), the SPP propagation constant is close to k_0 and the waves extend over many wavelengths into the dielectric space. In the opposite regime of large wave-vectors, the frequency of the SPPs approaches the characteristic *surface plasmon frequency*:

$$\omega_{sp} = \frac{\omega_p}{\sqrt{1 + \epsilon_2}} \tag{1.38}$$

as ω approaches ω_{sp}, wave vector tends to infinity and group velocity goes to zero. In this case oscillation mode acquire electrostatic character and is called *surface plasmon*. Such mode is obtained when $\epsilon_m(\omega) + \epsilon_d = 0$.

Real conductor Excitations of the conduction electrons in real metals suffer both free-electron and inter-band damping. Therefore, $\epsilon_m(\omega)$ is complex, and so the SPP propagation constant. In this situation travelling SPP are damped with a propagation length $L = (2Im[\beta])^{-1}$ (typically in the range $10 \div 100\mu m$) and reach a maximum, finite wave-vector at the surface plasmon frequency ω_{sp}. In this way there is a lower limit for the wavelength $\lambda_{sp} = \frac{2\pi}{Re[\beta]}$ and for the amount of mode confinement perpendicular to the interface, since the SPP fields fall off in the dielectric as $e^{-|k_z||z|}$ with $k_z = \sqrt{\beta^2 - \epsilon_2(\frac{\omega}{c})^2}$.

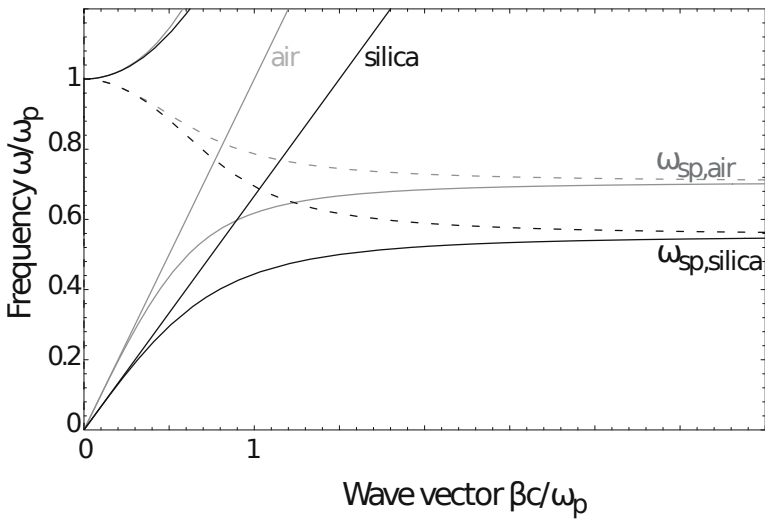

Figure 4: Dispersion relation at air/Drude metal and silica/Drude metal interfaces for dispersionless metals. Solid and dashed curves represent respectively $Re\{\beta\}$ and $Im\{\beta\}$ while straight lines represent light lines $\omega = kc/n$

It's important to stress the fact that SPP cannot be excited direct with three-dimensional light beams, since the propagation constant β is greater than the wave vector k inside the dielectric, leading to evanescent decay on both sides of the interface. There are various techniques for coupling radiation with SPPs like *prism coupling* and *grating coupling*. This last coupling will be used in the present work and described in the following.

1.2.3 Localized surface plasmons

Another type of surface plasmons can be defined, characterized by non propagating charge density oscillations, thus called *Localized surface plasmons*. LSP arise when oscillations are confined to metallic nanoparticles or nanostructures. When light interacts with metallic particles, smaller than the incident wavelength, the electrons of a nanostructure can couple to the electromagnetic field. The curved surface of the particle exerts a restoring force on electrons, so that resonances may arise when the particle is placed in an oscillating EM field. This leads to field enhancement both inside the particle and outside, in the adjacent sub-wavelength region. In contrast to SPPs, LPSs can be excited by direct light, without particular technique. The frequency of the resonance depends on the metal, the shape and the size of the particle, and also from the dielectric constant of the medium embedding the nanoparticles. In general there is not analytic model describing this resonances. For spherical particles the Mie theory [10] allows a full treatment of the scattering problem by a single non-interacting spherical particle, expanding solution in spherical multi-pole partial waves. In

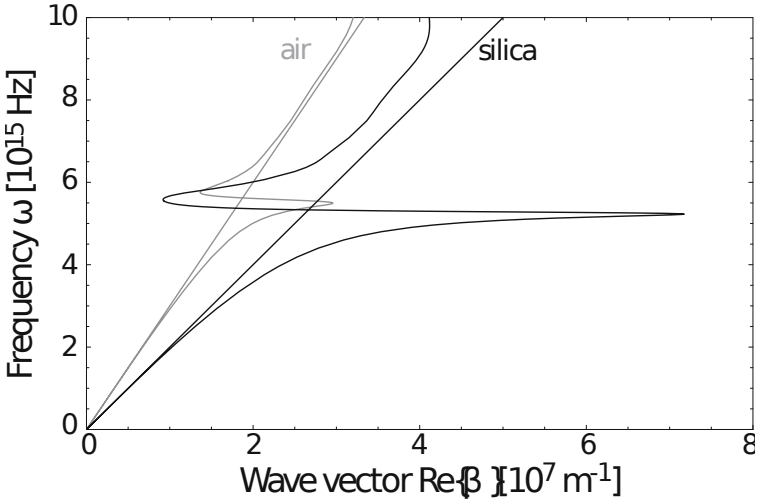

Figure 5: Dispersion relation at air/metal and silica/metal interfaces for real metals (silver in this case).

the dipole approximation, for particles smaller than both radiation wavelength λ and inter-particles distance d, two different regimes are found: if $d \ll \lambda$ the *near-field* interaction dominates with a d^{-3} dependence and strong field localization occurs between adjacent particles. If $d \gg \lambda$ far field dipolar coupling dominates, with d^{-1} dependence.

1.3 Nanohole arrays and the EOT

This work focus principally on the properties of nanohole arrays in metal films and their possible applications. These nanostructures present a special optical property, the *extraordinary optical transmission (EOT)*, first described by Ebbesen in 1998 [4]. This phenomenon consist in an enhancement of the EM radiation transmission through a metallic nanohole array of sub-wavelength size, i.e. more light can pass through the apertures than incident on their areas.

1.3.1 Transmission by sub-wavelength apertures

The starting point to study the transmission through apertures, is the description of the diffraction by a single hole in an opaque screen. In this situation if the radius of the aperture is larger than the wavelength of the impinging radiation ($r \gg \lambda$), the problem can be treated with Huygens-Fresnel principle and the light transmitted is almost the total light incident in the hole area, thus the *transmission coefficient* is about to 1. The more interesting case is the sub-wavelength one, in which $r \ll \lambda_0$, because near-field effects are expected to dominate the response. Bethe and Bouwkamp [11]first considered such a system assuming that the film was infinitely thin and a perfect conductor. For normal

incidence the aperture can be described as a small magnetic dipole located in the plane of the hole and the transmission coefficient becomes:

$$T = \frac{64}{27\pi^2}(k_0 r)^4 \tag{1.39}$$

where $k_0 = 2\pi/\lambda_0$. The scaling with $(r/\lambda_0)^4$ implies very weak total transmission and is in agreement with Rayleigh's theory of the scattering by small objects.

If the hypothesis of infinitely thin screen is relaxed, assuming a finite thickness h, via numerical simulation [12]it is found that the transmission coefficient is exponentially attenuated with h. At least if the real character of the metal is taken into account, with finite conductivity, the screen is not perfect opaque, but if h is on the order of several skin depths, radiation tunnelling is prevented.

Bethe also predicted that the light would be diffracted as it emerges from the hole in an angular pattern that depends on the orientation relative to the polarization of the incident light. If the diffraction pattern is scanned along the direction of the incoming polarization the intensity should be constant, while in perpendicular direction, the intensity decreases with increasing angle [11].

Mesurements of transmission and diffraction from a single sub-wavelength aperture revealed unexpected features: less diffraction intensity and the presence of a peak in the transmission spectrum (Wood's anomalies) [13]. The appearance of these resonant peaks can be understood as the excitation of SP modes at the edges of the hole, in particular LSPs in this case. In general it is often the presence of some type of resonance that leads to transmission enhancement [14].

1.3.2 Grating coupling

The mismatch in wave-vector between the in-plane momentum $k_x = ksin\theta$ of impinging photons and β can be overcome by patterning the metal surface with a shallow grating of grooves or holes with constant lattice a. The ordered array can be described via a primitive cell and a basis vectors: this configuration produces a reciprocal lattice, whose vectors provide the momentum needed for SPP excitation. For the simple one-dimensional case, phase-matching takes place whenever the condition:

$$\beta = ksin\theta \pm \nu g \tag{1.40}$$

is fulfilled, where $g = \frac{2\pi}{a}$ is the reciprocal vector of the grating and $\nu = 1, 2, 3, ...$ The excitation of SPPS is detected as a minimum in the reflected light. The reverse process can also take place: SPPs propagating along a surface modulated with a grating can couple to light and thus radiate.

For one-dimensional gratings, significant changes to the SPP dispersion relation occur if the gratings are sufficiently deep, so that the modulation can no longer be treated as a small perturbation of the flat interface. In fact localized modes inside the grooves lead to distortions of the first higher-order band [15].

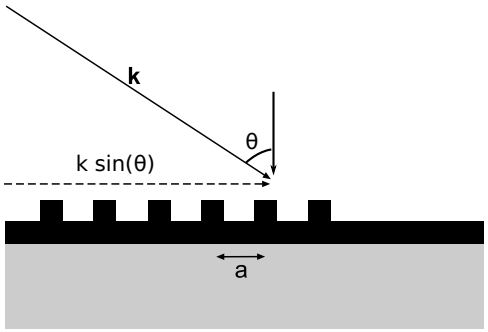

Figure 6: Grating coupling between light and SPPs.

1.3.3 Extraordinary transmission in nanohole arrays

As pointed out before, metallic structures can convert light into SPs by providing the necessary momentum conservation for the coupling process. If a screen with regular, periodic lattice of holes is structured, the phase-matching conditions imposed by the grating leads to a well-defined structuring of the transmission spectrum $T(\lambda_0)$, with peaks at the wavelengths where excitation of SPPs takes place. At these wavelengths, more light can tunnel through the aperture than incident on their area, since light impinging on the metal screen is channeled trough the aperture via generation and propagation of SPPs. This is the so called *extraordinary optical transmission, EOT*.

This enhanced transmission is the result of a resonant coupling of the EM radiation which impinges the metal, with standing surface plasmons on both sides of the film. The process can be divided into three steps: the coupling of light to SPs on the incident surface, transmission through the holes to the second surface and re-emission from the second surface. The intensity of SP electromagnetic fields above each holes compensates for the otherwise inefficient transmission through each individual hole.

The observed structure of $T(\lambda)$ can be explained by assuming that grating coupling to SPPs takes place, with the phase matching condition:

$$\beta = k_x \pm nG_x \pm mG_y = ksin(\theta) + (n+m)\frac{2\pi}{a} \tag{1.41}$$

where k is the incident wave-vector and θ the incidence angle, G_x and G_y are basis wave-vectors of the reciprocal lattice and n, m are Miller indexes which define scattering order, thus direction of propagation of the excited SPP.

Considering the case of a two-dimensional triangular array, the peak positions λ_{max} at normal incidence are given in a first approximation by the Bloch-wave SPP relation [16, 17]:

$$\lambda_{SPP} = \frac{a}{\sqrt{n^2+mn+m^2}}\sqrt{\frac{\epsilon_m\epsilon_d}{\epsilon_m+\epsilon_d}} \tag{1.42}$$

where a is the period of the array. As this result is valid for negligible holes' diameter and the associated scattering losses, it neglects the interference that gives rise to a resonance red-shift, so more accurate relation would be necessary.

To quantify the extraordinary transmission is worth to define a normalized transmission coefficient T_{norm} as the ratio between transmittance T_{NHA} and the sum of that for the single holes T_{SHj}:

$$T_{norm} = \frac{T_{NHA}}{\sum_j T_{SHj}} \tag{1.43}$$

When extraordinary transmission occurs T_{norm} becomes greater than 1 for the wavelength at which there is a resonance between EM radiation and SPPs.

Features of NHA The SPs generated in the array will propagate along defined symmetry axes with their own polarization depending on the (n, m) number of the mode, and then is been re-emitted to far-field. Interesting is the way in which this happens: one can suppose that the SPP emerging from the holes propagates on the metal surface and are scattered by the array of holes, so the strength of the enhancement depends on the number of scattering centres encountered by the SPP within his decay-length. Instead a study [18] on mini-arrays demonstrates that is only the local environment which influences the extraordinary transmission, because excited SPPs are confined to the immediate surroundings of the emerging hole and scattering from only nearest neighbours, generating standing waves.

Furthermore relation (1.42) is valid for a single interface between two semi-infinite layers, but the nanohole array presents two interfaces, that can both sustain SP modes. So if the two surfaces are in contact with different materials, the transmission spectrum contains two sets of peaks, each set belonging to one of the surfaces.

An interesting feature of the nanohole arrays is that, as it's clear from (1.42) despite the rough approximation, there is a linear relationship between the periodicity of the array a and the position of the peak, so tuning this trait permits to choose the position of the peak.

Other important properties to control the transmission spectra are:

Thickness h Two cases need to be distinguish: if the skin depth δ is larger or of the order t, SPPs excited by incident radiation on front interface might couple with SPPs on the other, only if adjacent dielectric is the same. If $t \gg \delta$, as happens in this work for Vis-NIR, there is no transmission through the metal film and the radiation can only tunnelling through the holes via SPPs.

Hole diameter d If the diameter is large enough to allow propagating modes, transmission could be modulated via resonances of wave-guide modes. But when $d \leq \lambda/2$ only tunnelling modes are allowed. In this work this condition is generally fulfilled, since $d \lesssim 800nm$ and typical resonance is at $\lambda = 1540nm$.

Holes diameter is also important in determining the line-width of the peaks, in fact reducing the diameter makes the Wood's anomalies shaper and contributes to obtain well-defined peak, but reduces the transmission [18].

Hole simmetry Different spectra are observed with square rather than circular holes, in particular square holes spectra strongly depend on the polarization of the impinging light [14].

LSP modes Another phenomenon to point out is the rise of localized surface plasmons modes on the rim of each hole, due to the strong localization of the field. The emission spectrum is influenced in two ways by this hot-spots: hole's effective diameter results increased and with it the cut-off wavelength limit for propagating modes allowed inside the hole, and field enhancement at the rim, which can increase the transmission. Besides, a study of Degiron and Ebbesen [19] pointed out that the contribution of the LSP modes is less important than that of propagating SPP.

2 Nanohole array fabrication

There are many techniques used to produce nanohole arrays. One fundamental feature they must have is the possibility of controlling dimensional parameters of the nanohole array during the synthesis. The one adopted in this work is also a cost-effective way, characteristic which can be important in the eventually use for mass-fabrication of NHA based devices.

2.1 Nanosphere Litography

Nanosphere lithography (NSL) is an inexpensive, simple to implement, high throughput, self assembly technique capable of producing an unexpectedly large variety of nanoparticle arrays with controlled shape, size, and inter-particle spacing. It is based on the self-assembly of a monolayer of size-mono-disperse spherical nanoparticles of polystyrene to form a colloidal crystal on the substrate surface. NSL particle diameters ranging from 40 nm to several microns and the size of the polycrystalline monolayers can extend up to several cm^2, and this is one of the main advantages of this technique [20, 21]. These monolayers, arranged with HCP crystalline structure, can be used as efficient templates to fabricate 2-D ordered nanostructure arrays in particular as a mask for the metal deposition [22].

Mechanism of masks formation Closed-packed monolayers of colloidal spheres can be produced by spreading particles solution on a solid surface and evaporating the solvent. The formation of the monolayers of colloidal spheres is due to the lateral capillarity forces that acts when the spheres protrude from the solvent. The spheres are pushed together and nucleate an ordered mono-layer, flow of solvent brings in more spheres and the mono-layer grows. The nature of the forces governing the ordering is revealed by the fact that 2D crystallization always starts when the thickness of the water layer becomes equal to the particle diameter.

Observations suggest a two-stage mechanism: at first stage, a nucleus of ordered phase forms. Spherical particles partially immersed in a liquid layer deform the liquid-gas interface, giving rise to strong and long-range inter-particle capillarity forces. These attractive forces are caused by two effect: *pressure effect* caused by hydrostatic pressure and *surface force effect* due to the spatial variation of the slope of the liquid surface. Energy of capillarity attraction can be much larger than the thermal energy, k_BT, even with sub-micrometer particles, and interaction is a long range force, whose effect extend at distances greater than 1000 particles radii.

Once the nucleus is formed, the second stage of crystal growth starts through directional motion of particles toward the ordered array. This motion is caused by a convective water flux which carries along the particles toward the ordered phase. Once ordered regions are formed, the thinning of the water layer inside them is slowed due to hydrophilicity of the particles. The evaporation from the menisci between the particles, clustered in a nucleus, increases the local

curvature and hence the local sucking capillarity pressure. A convective influx tends to compensate the water evaporation and carries the particles toward the clusters, where they remain attached to the domains, pressed by hydrodynamic pressure and captured by capillarity attraction [23].

Experimental procedure Among the variety of methods that can be used for deposition of the nanoparticles on the substrate, the chosen one for the present work is based on the works of Schatz and uses a colloidal suspension of polystyrene (PS) nanospheres in ultra-pure water and alcohol (2-Propanol).

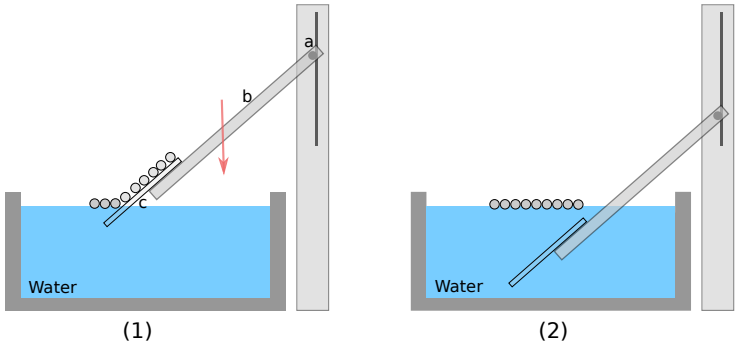

Figure 7: The device used for self-assembling mask consists of a rack and pinion system (a) driven by a small electric engine that allows to the T-shaped arm (b) to move vertically at two different speeds. At the end of the arm a SLG substrate (c) is fixed and NSs are deposided on. As the substrate is dipped, in (1), NSs separate from it and start floating on water surface. In (2) a well-ordered monolayer of NS has formed.

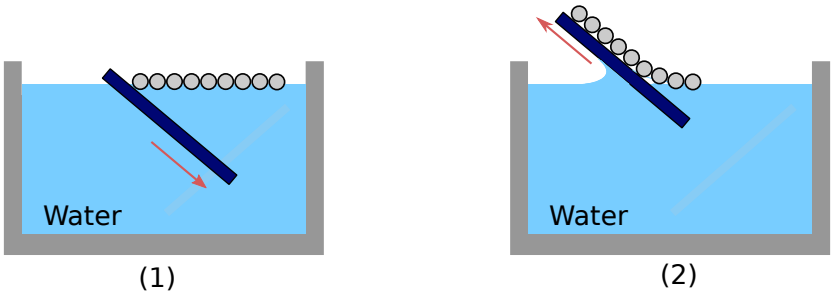

Figure 8: Collecting step is here showed. A second substrate is used to manually pick up the monolayer by first dipping it in the water then slowly pulling it out together with the NS mask.

The first step is the cleaning of the substrate in a "Pirahna" solution, to make the substrate hydrophilic: at first an acid solution is used, a 3 : 1 mix-

ture of concentrated sulphuric acid with 30% hydrogen peroxide, and after a basic one, $3:1$ mixture of concentrated ammonium hydroxide with 30% hydrogen peroxide. The substrate is then rinsed with Milli-Q water and dried in a stream of nitrogen. The suspension of PS nanoparticles and isopropylic alcohol is poured on the clean substrate and slowly immersed in a large glass vessel filled with Milli-Q water. PS particles self-assemble at the meniscus between alcohol dispersion and water bath, the resulting compact monolayer floats on the water surface, and it is collected on the substrate surface and slowly pulled out and dried at room temperature.

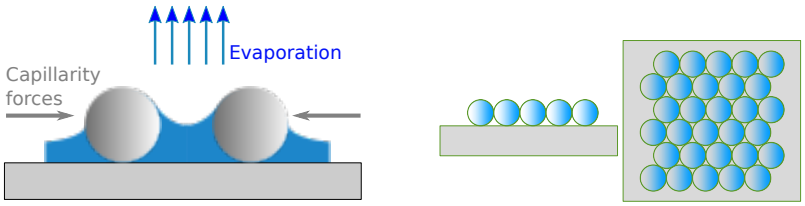

(a) Drying step, while capillarity forces drive the monolayer to a close-packed pattern.

Figure 9: Self-assembled monolayer of PS nanospheres

During different depositions some parameters had been varied, to optimize the formation of an extended and ordered monolayer on the water surface and to collect it.

Dilution of the solution Different dilutions are used for the water/alcohol nanospheres solution, to change the evaporation rate, and finally the chosen one was a $1:1$. In fact with the others tried ($1:2$ and $3:4$) no mask were formed on the water surface.

Water temperature The temperature of the water bath was varied to modify the dispersion of the mask on the surface, for $D = 248nm$ cold water ($4°C$) was better to form a good mask, instead for $D = 1030nm$ room temperature was chosen.

Volume of solution The volume of the poured solution was varied between $30\mu l$ and $90\mu l$ and the quantity necessary to form a sufficently wide mask was found to be $75 \div 85\mu l$.

Enviromental conditions Is worth noting that environmental conditions have strong influence on the formation of good mask, in particular temperature and humidity. Typical conditions are a temperature of $20°C$ and humidity of $\sim 60 - 70\%$.

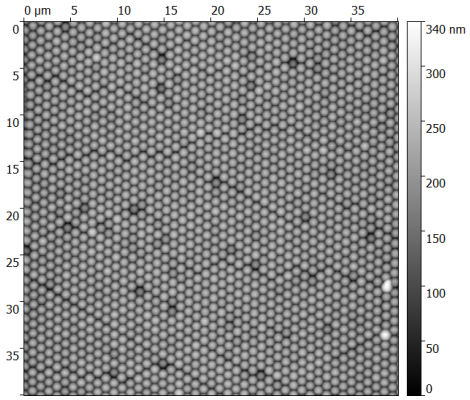

(a) AFM image of a self-assembled mask of nanospheres

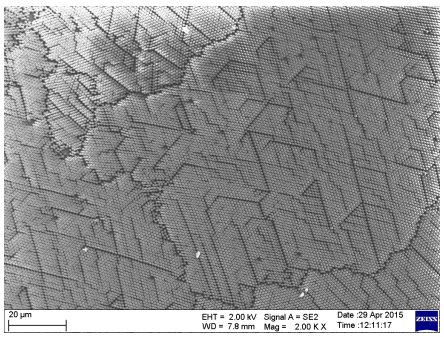

(b) SEM image of a self-assembled mask of nanospheres

2.2 Reactive ion etching

For the fabrication of the NHAs, is needed a reduction of the diameter of the PS nanoparticles of the colloidal crystal, keeping unchanged the lattice position of the spheres, to obtain a 2D periodic non-closed-packed array of PS nanoparticle, that will be used as a mask for the subsequent metal deposition.

Reactive ion etching (RIE) is a plasma-based dry etching technique characterized by a combination of physical sputtering with the chemical activity of reactive species.[24] The etching is anisotropic and chemically selective, and the gas mixture determines the etched species. The etching rate has to be controlled, to choose the correct nanopartice size and optimize the features of the NHA obtained from the mask.

RIE parameters The most important parameters controlling the etching rate are the gas composition, plasma energy and working pressure. The gas chosen

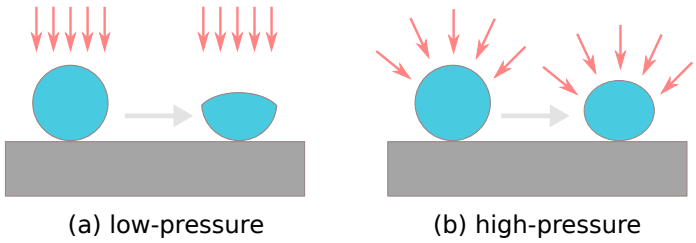

Figure 10: The two types of RIE etching, according to the pressure.

was a mixture of Ar (28%) and O_2 (72%), where O_2 acts as active chemical species. Some parameters have been varied in order to reach an optimum condition. Three different pressure have been studied: high ($\sim 3700 \cdot 10^{-4} mbar$), medium ($\sim 800 \cdot 10^{-4} mbar$) and low ($\sim 80 \cdot 10^{-4} mbar$); and with powers between $10W$ and $20W$, in general the higher the power, the faster is the etching rate. In particular at high pressure (HP) the chemical action is enhanced and we obtain particles with a more homogeneous surface, but the particles were eroded even in the bottom surface, so often they dropped and moved from original position. At low pressure (LP) instead, physical action was prevailing, so the erosion was less homogeneous, but particles remain more stable in their lattice site.

Pressure	$9 \cdot 10^{-3}$mbar
O_2 flux	3.7 sccm
Ar flux	1.2 sccm
Bias	199 V
Power	12 W

Table 2: Optimal parameters for low-pressure RIE process used in the present work.

2.3 Metal deposition

Once obtained the 2D periodic array of PS nanoparticles and etched it, the mask can be used as a template for the metal deposition. The metal deposition was performed with a magnetron sputtering system, which consist in the physical removal of material from a target (metallic in this case) by the collision of inert atoms. Atoms from an ionized gas (e.g. Argon) strike the metallic target eroding it, this caused the ejection of atoms from the target in all directions [25]. Ejected atoms reach the sample through diffusion in an evacuated chamber and deposit there, growing the desired metallic layer.

Clearly since source has finite dimension, emission of the target atoms is neither spherically nor uniformly distributed, so the sample was placed in front of the source, parallel to the target surface, and near the target to have a collimated sputtered atom flux, that reproduces the pattern of the etched mask.

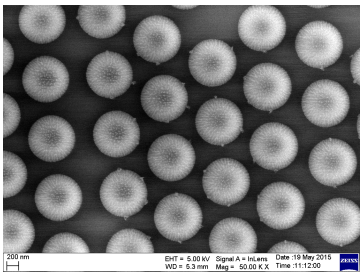

(a) 7 minutes RIE on $D = 1030nm$ diameter mask nanospheres

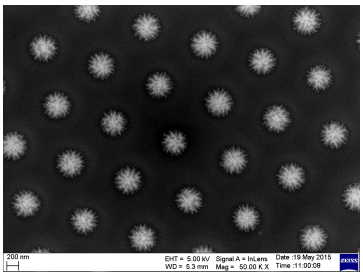

(b) 14 minutes RIE on $D = 1030nm$ diameter mask nanospheres

Figure 11: RIE tests with different exposure time

The power was kept as low as possible to avoid the heating of the sample and the melting of the PS nanospheres. The deposition took place in an Ar atmosphere, at a pressure of $510^{-3}mbar$ and with a power of $20W$. The metal will deposit both on upper surface of the particles and on the surface of the substrate, in the gap region between the etched spheres.

Mask remval After the deposition the mask was removed using ultrasound sonication in toluene, leaving a metallic nanohole array on the sample surface.

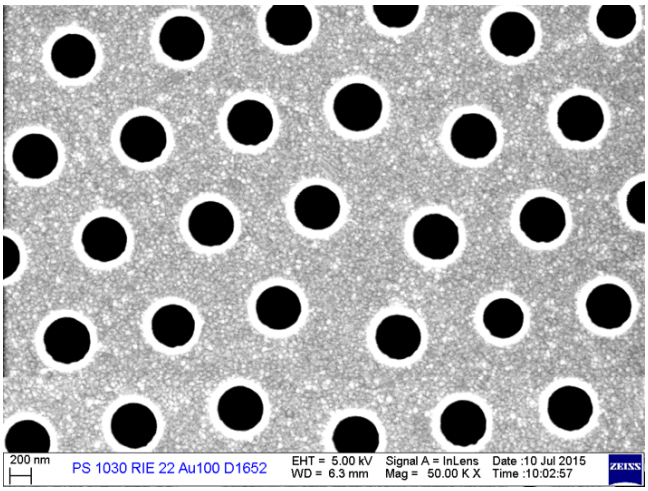

Figure 12: SEM image of a nanohole array after the mask removal process. The diameter results $D = 438nm$.

3 Characterization and results

Since the purpose of this work is the study of the interaction between plasmonic nanohole arrays and Erbium photo-emission, is necessary to find out the correct features for the NHA, that allow to have a correct matching between resonance peak of the EOT and the characteristic Er transition ${}^4I_{13/2} \rightarrow {}^4 I_{15/2}$, at $1.54\mu m$. In order to do this, numerical simulation have been carried out.

3.1 FEM simulations

Is necessary to find the correct lattice parameter that allows to have a resonance EOT peak at about $1.54\mu m$; to do this Finite Elements Simulation (FEM, see section 6.3) have been performed. In order to simulate the NHA, the whole domain is constituted by silica, except for the NHA film extending in the XY plane, and centred at z=0, as shown by Fig. **??**. The translational invariance in the XY plane doesnt hold and it has to be replaced with the periodic Honeycomb lattice resulting from the NSL process.

The result from this numerical calculations was that the best value of the lattice parameters, that allows to have a good superposition between the Er emission peak and the EOT peak of the NHA, was $\sim 1\mu m$. The EOT peak in the simulation, therefore, results in good agreement with the experimental position when the chosen diameter of the nano-spheres for the mask was $1030nm$, so this size was chosen for the next experimental measurements.

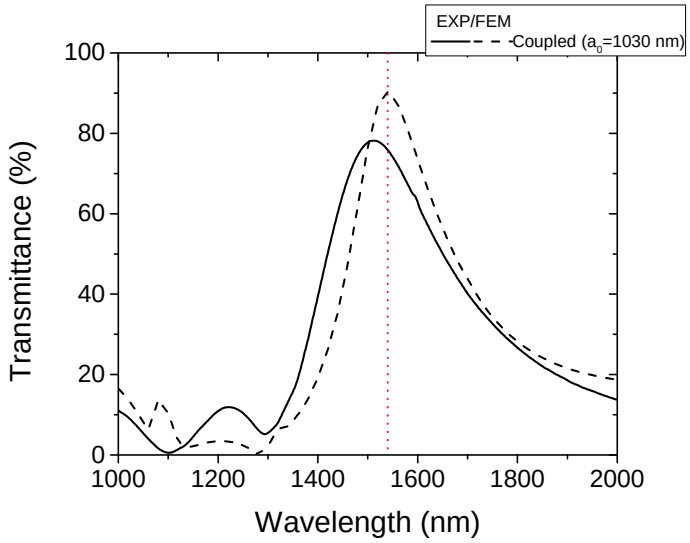

Figure 13: Comparison between the EOT peak obtained from FEM calculations and from experimental transmittance measurements on sample S_2. It's also reported the Er emission peak at $1540nm$.

3.2 Sample synthesis and features

3.2.1 Nanosphere masks

For the preparation of the NSL masks, polystyrene nanoparticles from Microparticles GmbH were used, in particular mono-disperse nanospheres of diameter of $(1030 \pm 12)nm$ in aqueous solution. The solution of nanoparticles suspension was prepared with isopropyl alchol (2-propanol).

For the mask synthesis three kind of substrate were used: Soda Lime Glass (SLG), hyper-pure silica glass (HSQ 300) and mono-crystalline silicon wafer with $< 100 >$ lattice orientation. SLG slabs were used only for the immersion while silicon and silica glass as substrate for the self-assembling of the masks.

After the cleaning in the "piranha" solutions, before the acid one for 1 hour treatment followed by the basic for a 20 minutes one, the substrates are ready for the self-assembly process.

A motorized dipper, shown in fig 14 was used for the immersion: the SLG substrate was fixed to the end of the T-shaped arm, the solution was poured over it, and it was slowly dipped into the water. Nanoparticles floating form a closed-packed mask, which was picked up using Si or SiO^2 slab and let drying.

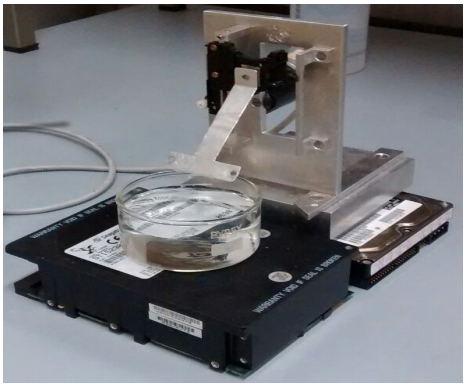

Figure 14: The mechanism employed for the self assembly.

Characterization In order to check the quality of the masks, two types of measurements were done, optical and morphological. Optical measurements were done using a *Jasco V-670 UV-VIS-NIR* spectrophotometer, by illuminating the sample with normally incident non-polarized light. Morphological characterizations were done by Atomic Force Microscopy (AFM) employing a *NT-MDT Solver PRO-M* microscope and by Scanning Electron Microscopy using *Zeiss SIGMA HD SEM-FEG* microscope. The absorbance spectra of the PS nanospheres masks were acquired, as in figure 15. The absorbance A is linked to the transmittance T (in percent) by the following relationship:

$$A = 100(2 - log_{10}(T)) \tag{3.1}$$

where both quantities are expressed in percent. In the NIR range the mask is almost transparent to the radiation ($A \lesssim 1\%$), but the absorbance increases quickly as λ decreases. The spectra present a sharp peak at about $1250nm$, and its width is linked with the overall degree of order of the mask. Therefore a narrow peak suggests a well-ordered mask.

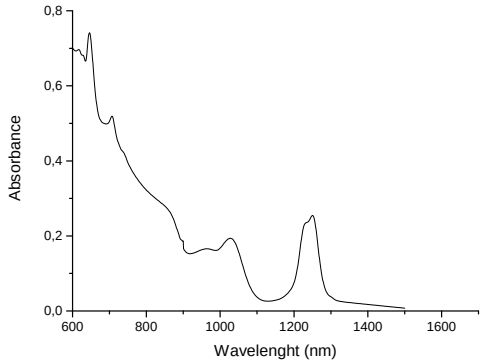

Figure 15: Absorbance spectrum of a 1030 nm PS nanospheres monolayer mask on silica.

More specific details about the morphology of the mask, but focused on a small area of the sample, were acquired by SEM and AFM microscopies. Figure 16 shows a SEM image of a mask produced by PS nanospheres of diameter of $1030nm$.

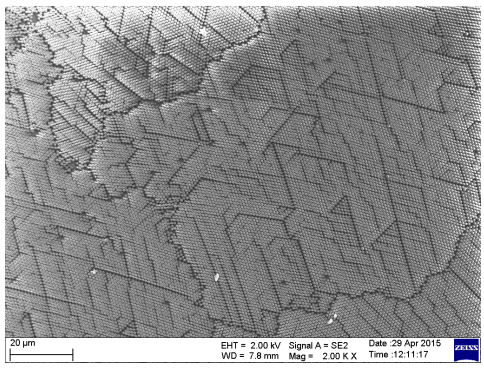

Figure 16: SEM image of a typical PS nanosphere mask

Figure 17 shows an AFM image of a mask, and its Fast Fourier Transform (FFT) calculated by Gwyddion software. The presence of a hexagonal lattice

of spots in the FFT image, representing the reciprocal lattice, suggests a well ordered array in the direct space.

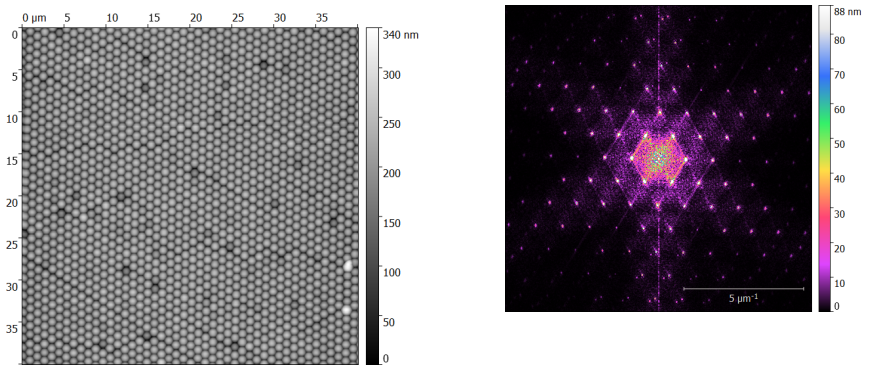

(a) Image of the direct lattice of the mask

(b) Fourier transform of the lattice

Figure 17: Images from AFM microscopy of PS nanospheres array.

These images show that the self-assembly of PS nanospheres allows to produce well-ordered monolayers.

3.2.2 Reactive ion etching

The RIE process was optimized to obtain the best size for the particles and to avoid their fall, caused by excessive erosion in the bottom part. The parameters chosen where reported in the table 2 and fixed them, the only free parameter to control the diameter of the etched particles is the etching time. Different RIE times were tested and a time calibration was done in order to control the etching rate, the etched masks were observed bye FE-SEM and the average diameter for each etching time was calculated by analysing the images with the ImageJ software.

Etching time (min)	Diameter (nm)	Fraction of initial size
0	1030 ± 12	1
12	790 ± 5	0.77
18	576 ± 4	0.56
22	498 ± 8	0.48

Table 3: Diameter of PS nanospheres after RIE process.

In the figure is reported a linear fit of the diameter as a function of the etching time, clearly the trend is not linear, but this allow to have a rough estimation of the etching rate. The etching time chosen, which allows to obtain the minimal diameter for the sphere and avoids their collapse, was of 22 minutes.

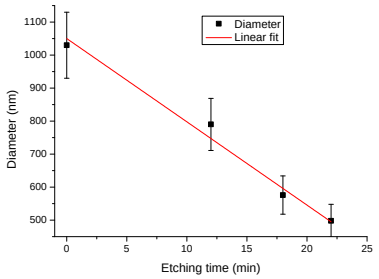

Figure 18: Plot of etched diameter against etching time.

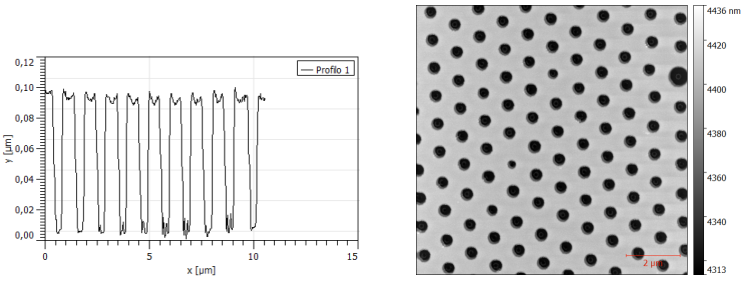

(a) AFM profile of NHA (S_1)

(b) AFM image of NHA (S_1)

Figure 19: AFM characterization of S_1.

3.2.3 Metal deposition

The metal film used for the samples is a gold film of $\sim 100nm$ deposited by the magnetron sputtering with an RF source. This thickness allow to ensure a quite good opacity to the film, at the typical frequencies used in this work of about $1.5\mu m$. The skin depth can be calculated as the reciprocal of the extinction coefficient (1.17), obtaining:

$$\delta = \frac{1}{\alpha} \approx 12nm \tag{3.2}$$

Considering as a good optically thick film the case in which it is at least 5δ thick, a $100nm$ thickness is enough to have a good screen.

The fixed parameters for deposition are reported in the table below:

The deposition time chosen for the samples in this work is of $6'45''$ and produced a thickness of $(93 \pm 2)nm$ for the sample S_1 used for the next characterizations. The thickness was measured with the AFM.

Pressure of the chamber	Power	Deposition rate
$5 \cdot 10^{-3} mbar$	$20W$	$\sim 14nm/min$

Table 4: Set for the magnetron sputtering.

3.3 NHA characterization

The NHA characterization is optical and morphological, in order to obtain informations on both the structural features and the optical transmission and to understand the correlation between them.

Morphological measurements The structural characterization is based on the SEM images, which allow to measure the diameter of the holes and to evaluate the roughness of the surface, as well as the smoothness of the holes' rim.

The measured diameter of the holes for the test samples S_1 and S_2 are reported in table below:

Sample	Time of RIE (min.)	Holes' diameter (nm)
S_2	18	552 ± 10
S_1	22	438 ± 8

Table 5: Holes' diameter correlation with RIE duration.

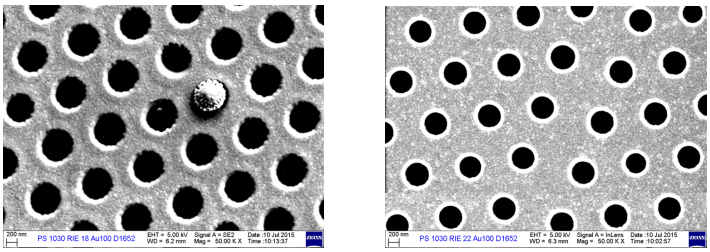

(a) Sample S_2, RIE time $18min$ (b) Sample S_1, RIE time $22min$

Figure 20: SEM images of NHA.

As it's clear from the images the roughness and irregularity in the sample S_2 are more evident than in sample S_1, so the last is chosen as model for standard fabrication in the following of the work.

Optical spectra In order to evaluate the extraordinary transmission for the nanohole arrays, optical spectra were acquired using the *Jasco V-670 UV-VIS-NIR* spectrophotometer. The spectra of sample S_1 and S_2 are shown in the figures below.

It's evident the presence of a transmission peak at $\sim 1500nm$ for S_1 and at $\sim 1700nm$ for S_2. Being the lattice constant the same (it is determined by the initial diameter of the nanospheres, which was $1030nm$), the spectra show a red-shift of the transmission peak as the diameter of the holes increases. Moreover appears an obvious reduction of the transmission efficiency and also a sharpening of the peak while the diameter decreases.

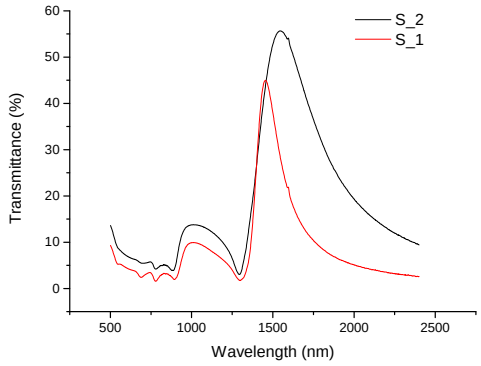

Figure 21: Optical spectra for samples S_1 and S_2.

EOT measurements The EOT peak, corresponding to the $< 1, 0 >$ SPP Bloch-wave excitation, is observed in the NIR range. To define the position of a peak, its centroid can be used, that corresponds to the center of mass of the peak. The wavelength of the centroid of the EOT curve in such a spectrum is given by

$$\lambda_{centroid} = \frac{\sum_i \lambda_i (T_i - T_{th})}{\sum_i (T_i - T_{th})} \tag{3.3}$$

where T_i is the transmittance at the wavelength λ_i, T_{th} is a threshold value of transmittance chosen between the peak minimum and the maximum, and only λ_i such that $T_i > T_{th}$ are considered in the evaluation of $\lambda_{centroid}$. Centroids are measured in a range from $1350nm$ to $2500nm$, and results for S_1 and S_2 are reported below.

Sample	Centroid (nm)	FWHM (nm)
S_2	1672	370
S_1	1566	177

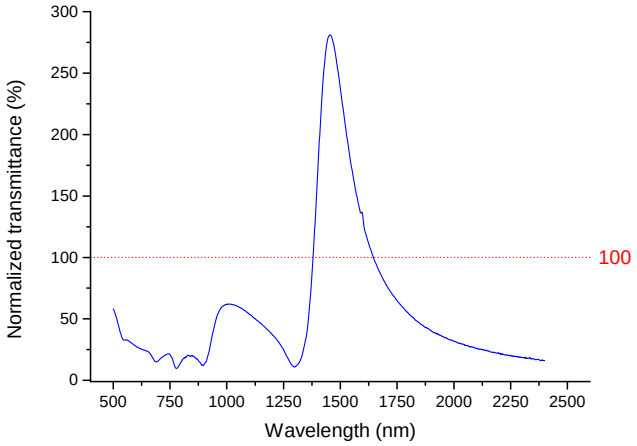

Figure 22: Normalized transmittance spectrum for sample S_1.

Normalized transmittance tells how much light passes through the NHA with respect to the light that would pass through a single hole, in an opaque screen, with an area equivalent to the sum of all the single apertures. Therefore, the normalized transmission is calculated as the ratio of the measured one to the filling factor f of the NHA, for sample S_1.

$$f = \frac{\text{Holes area}}{\text{NHA Area}} = \left(\frac{d}{2a_0}\right)^2 \frac{2\pi}{\sqrt{3}} \approx 0.16 \tag{3.4}$$

where d is the hole diameter and a_0 is the periodicity of the array. It means that, neglecting plasmonic properties, 16% of the incident light would be transmitted. Dividing the transmittance spectrum by f, the plot from figure **??** is obtained. Transmittances above 100% can be observed and this stresses that an extraordinary transmission occurs through the NHA.

3.4 Conclusions

The presence of an extraordinary optical transmission resonance through plasmonic nanohole arrays has been demonstrated. This EOT is due to the coupling between impinging EM radiation and SPP Bloch-waves, which can propagate through the holes and being re-emitted to the far-field.

The conditions for fabrication of the nano-structure have been optimized for the matching between the EOT resonance and the Er^{3+} typical emission peak at $1.54\mu m$, in order to study the mechanism of interaction between emitters and nano-structures, and evaluate the possible modifications in the photo-emission efficiency.

4 Er:SiO_2 films

Erbium doped materials are of strategic interest in the field of optical communication technology for their application in many photonic devices [6, 26–28]. This importance is related to the sharp room temperature luminescent emission at $1540nm$ of the Er^{3+} ions, that matches the window of minimum losses in silica optical fibres. This chapter will focus on the synthesis and the characterization of Er-doped silica thin films via co-sputtering, investigating the effects of the preparation parameters in order to optimize the photo-luminescence of Er^{3+} ions embedded in the silica matrix.

4.1 Er^{3+} optical properties

Erbium is a rare earth element in the Lanthanides series, with atomic number 68. The electronic configuration of the neutral Er atoms is $[Xe]-4f^{12}6s^2$, while the most common form of Er embedded in a solid is the ionic trivalent state Er^{3+}, which has an electronic configuration $[Xe]-4f^{11}$. Since Er ionization involves the removal of two weakly bounded $6s$ electrons and one of the $4f$ shell, Er^{3+} ion has an incompletely filled $4f$ electron shell shielded from external fields by outer-lying filled $5s^25p^6$ shells from the $[Xe]$ configuration. The electrostatic shielding of the $4f$ electron shell reduces the perturbation due to the charges of surrounding ligands and makes this shell quite atomic-like. Due to this fact atomic energy levels and hence spectroscopic properties can be understood from a consideration of the free ions [29].

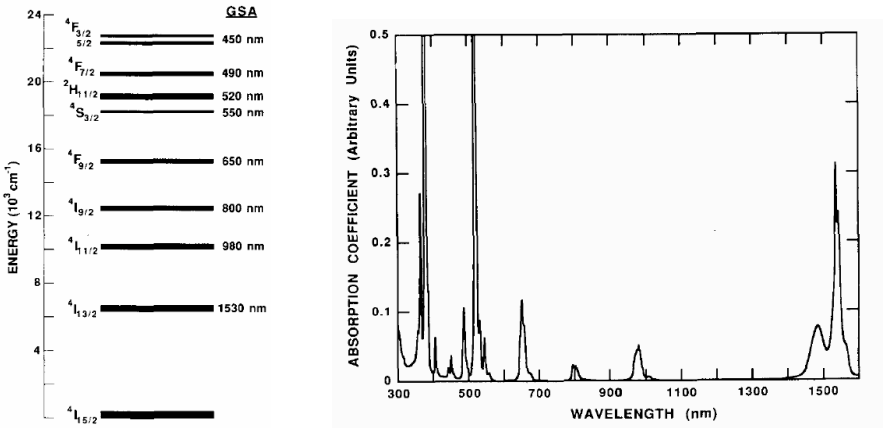

Figure 23: (a) Energy levels of Er^{3+} labelled with the Russell-Saunders notation. For each state the GSA column lists the wavelength of the ground-state absorption transition terminating on it. (b) Absorption spectrum of Er-doped silicate glass. Absorbtion values at the peaks of the strong bands at 380 and 520 nm are 1.5 and 1.0, respectively [26].

In the case of the free ion the degenerate levels are sharp with equal parity and therefore the electric-dipole transitions involving one photon between most of these energy are parity forbidden. However, when Er ion is embedded in a host material the surrounding chemical species weakly perturb the $4f$ state, inducing odd-parity character in the $4f$ wavefunctions and allowing for the occurrence of radiative transitions.

PL emission spectrum The Er excitation process originating the characteristic ${}^4I_{13/2} \rightarrow {}^4 I_{15/2}$ transition at $1.54\mu m$ occurs with the absorption of a photon in one of the higher-lying levels, followed by the non-radiative fast multi-phonon decay to the metastable ${}^4I_{13/2}$ state ($\tau < 10ns$) [30]. The relaxation energy between the ${}^4I_{13/2}$ state and the ground state is about $0.8eV$, so multi-phonon emission is unlikely and the radiative emission occurs. The PL emission spectrum shape depends on the host glass, the peaks and valleys are determined by the locations of the Stark levels, the intensity of the transition between the Stark levels and the amount of inhomogeneous and homogeneous broadening of these levels [31].

Lifetime The lifetime (τ) of an excited level is given by the inverse of the sum of radiative (γ_r) and non-radiative (γ_{nr}) decay rates, according to the Mattiessen's rule:

$$\frac{1}{\tau} = \gamma_r + \gamma_{nr} = \frac{1}{\tau_r} + \frac{1}{\tau_{nr}} \tag{4.1}$$

The typical transition of Erbium is characterized by a large separation energy between the two levels, so the lifetime is in the millisecond range and mostly radiative, since the phononic non-radiative transition probability drops exponentially with the number of phonons required to bridge the energy gap. Anyway, the presence of matrix impurities and defects can act as non-radiative recombination centres and influence the decay rate of the non-radiative transitions. Moreover, the long lifetime of the metastable state, makes Er^{3+} emission sensitive to non-radiative decay process such up-conversion and concentration quenching.

Cross section The cross section quantifies the probability of the transition between two states to occur, with the concurrent emission or absorption of light. Optical transitions in Er^{3+} have small probability: the cross-sections for optical excitation and stimulated emission are quite small, typically on the order of $10^{-19} - 10^{-21} cm^2$ depending on the host matrix [6, 26, 32]. This on of the major limitations in the realization of photonic and optoelectronic devices with Er doped materials.

4.2 Er:SiO_2 film synthesis

Erbium-doped silica ($Er : SiO_2$) films were prepared via co-deposition of Er and SiO_2 in a magnetron sputtering system. A metallic Erbium target was mounted

on a magnetron Direct Current (DC) source while the SiO_2 one was placed on a magnetron Radio Frequency (RF) source. As sputtering gas a mixture of Ar and O_2 was used ($95\%Ar + 5\%O_2$), operating at room temperature and at a pressure of $5 \cdot 10^{-5} mbar$, which is the lowest one to sustain the plasma and to minimize the re-sputtering phenomenon. The reactive atmosphere was chosen to prevent a slight oxygen under-stoichiometry observed in pure argon depositions. The deposition was performed at $250W$ for the RF source (to prevent overheating of the sample) and at $3W$ for the DC one. The concentration of Er varies linearly with the power of the DC source and the film thickness shown a linear dependence with the deposition time at constant RF power.

4.3 Measurements on Er:SiO_2 films

To characterize the Er doped silica films, photo-luminescence (PL) spectroscopy measurements were used. A model of the apparatus is visible in fig.24. The measurements were done by exciting the sample with a $6Hz$ mechanically chopped continuous wavelength (CW) Ar laser (1), with in-resonance conditions ($\lambda_{exc} = 488Hz$), selected by a laser line filter. The chopper (3) was placed between two lenses (100 mm focal length) (2) to reduce laser beam spot dimension on the chopper plane and obtain a faster open/closed transition. Emitted radiation was collected by a single-grating monochromator (8) via two converging lenses (7). To detect the luminescence signal a near-infrared photomultiplier was used (HAMAMATSU R5509-72) (10) cooled by liquid nitrogen, and acquired with a lock-in amplifier, using the chopper frequency as a reference. Time-resolved analyses were performed by fixing the monochromator wavelength at $1.54\mu m$ and collecting the PL intensity evolution with time using a digital oscilloscope (Tektronix TDS 7104).

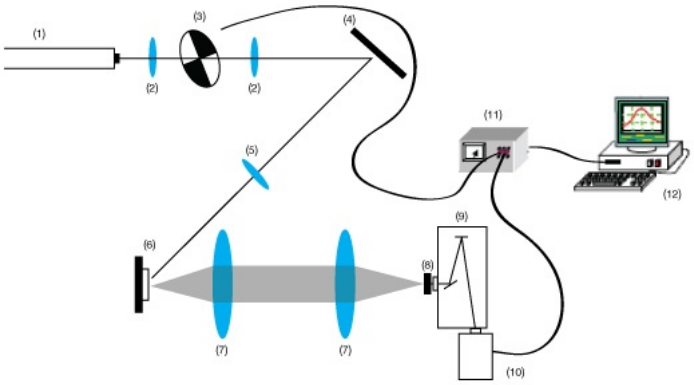

Figure 24: A schematic representation of the PL measurement set-up.

4.3.1 Thermal activation

After the deposition no luminescence signal was detectable in IR region, because of the local disorder around the Er ions. Defects like dangling bonds, vacancies, bond angle and length distortion in the silica network can act as non-radiative de-excitation centres, dampening the Er^{3+} emission. Annealing above the temperature of $400°C$ is required to recover host matrix defects and to restore the octahedral coordination of 6 oxygen atoms around the Er ions [33]. Temperature and atmosphere of the thermal annealing influence the restoring of the defects in the silica matrix and the promotion of the oxygen coordination around Er ions. In a simple picture the PL intensity (I_{PL}) can be described by the relation:

$$I_{PL} \propto N_{act}\eta \tag{4.2}$$

where N_{act} is the concentration of optically active Er ions and η is the quantum efficiency of the luminescence process, given by:

$$q = \frac{\gamma_{rad}}{\gamma_{rad} + \gamma_{nr}} = \frac{\tau}{\tau_{rad}} \tag{4.3}$$

with the measured lifetime τ and the radiative one τ_{rad}.

The condition chosen for thermal annealing were $900°C$ temperature and vacuum atmosphere, for a two hours treatment. This are the conditions in which a maximum is reached both for intensity and lifetime [34]. Above $600°C$ (minimum temperature for measurable signal), both intensity and lifetime increase rapidly, thanks to the restoration of the configuration order in the silica matrix and to the increase of the quantum efficiency of the radiative transition. PL intensity reaches a maximum at $900°C$ and decrease for higher temperature, because of the decrease of the number of optically active Er ions, due to the Er-Er clustering phenomenon, which is known to produce concentration-quenching of the PL intensity. Lifetime keep on increasing, but slower above $800°C$. Annealing in high vacuum, besides, increases by more than 3 times the PL intensity respect to air, suggesting that low pressure supports the out-diffusion of quenching species, as OH groups, from the deposition layer.

4.3.2 Er^{3+} spectrum

After the thermal annealing was possible to acquire PL spectra of the Erbium-doped films, obtained with the resonant excitation of Erbium using the $488nm$ laser line.

It's clearly visible the emission due to the transition from the first excited state to the ground ($^4I_{13/2} \rightarrow^4 I_{15/2}$) that presents a main peak at $1540nm$ (1), a shoulder at $1500nm$ and two weak structures at longer wavelength (2, 3). The peak centroid is located at $1542nm$ and the FWHM is $56nm$, the total width of the main peak and the long tails are due to the Stark splitting of the excited and the ground states in the host electric field, as well as homogeneous and inhomogeneous broadening.

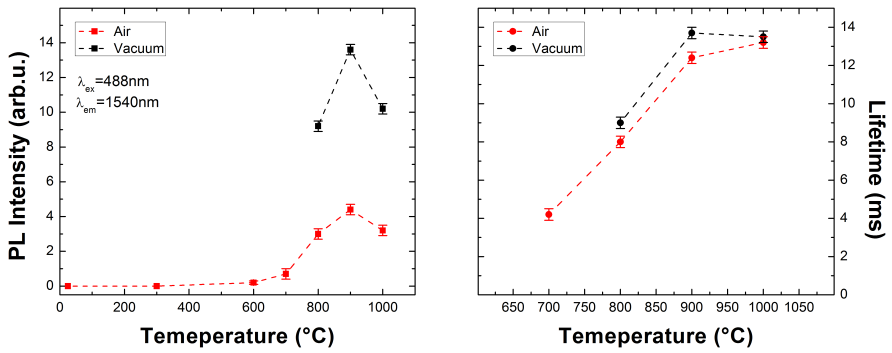

Figure 25: PL intensity (a) and lifetime values (b) at $1.54\mu m$ as a function of the temperature of the thermal tratments performed in air and in vacuum atmosphere [34].

In figure 27 the PL temporal intensity decay is shown, with a single exponential fit $I_{PL} = I_0 e^{t/\tau}$, where τ is the characteristic lifetime of the transition at $1.54\mu m$. The calculated lifetime results $(10.9 \pm 0.51) ms$. It's worth noting that this value is less than the one expected for pure radiative decay ($14.2 ms$ [6]), this probably due to the influence of a non perfect reconstruction of the matrix defects during the annealing process.

4.3.3 Er concentration

One of the problem in the use of Er-doped materials for photonic devices is the occurrence of concentration quenching phenomena. Concentration quenching is a manifestation of the Förster non-radiative energy-transfer phenomenon [35, 36], and causes a decrease in the luminescence emission as the concentration of emitting species increases. The mechanism proceeds through a self-energy transfer by a resonant interaction between couples of quenching centres. This migration becomes more efficient at smaller Er-Er distances, with an efficiency kt, which reads:

$$k_t = \frac{r^{-6}}{r^{-6} + R_0^{-6}} \tag{4.4}$$

where r is the separation between two Er ions and R_0 is the Föster radius, which depends on spectral overlap, refractive index of the matrix and relative orientation of emitters. Because of the rapid decay of the energy-transfer efficiency with increasing r, concentration quenching is significant only if r is less or comparable to R_0. For Er in silica the limit is reached for concentrations in the range $0.1 \div 1\% at$ depending on the matrix [37].

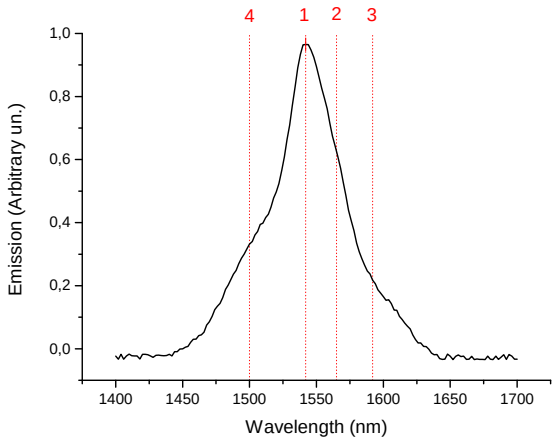

Figure 26: Main photo-emission peak for Er^{3+}. The various components of the peak are labelled.

4.3.4 Emission cross section

A fundamental parameter to characterize the optical properties of Er-doped systems is the emission cross-section. If the fluorescent bandwidth, the spontaneous lifetime and the degeneracy of the excited and ground states are known, the cross section can be estimated via the Fuchtbaner-Ladenberg equation[38]:

$$\sigma_{21} = \frac{\lambda^2}{8\pi\mu^2} A_{21} g(\nu) \tag{4.5}$$

where 1 and 2 are the ground and excited states respectively, and λ the wavelength of the peak, $g(\nu)$ is the line shape of the emission spectrum, A_{21} the Einstein coefficient for spontaneous emission and μ the refractive index. Considering only radiative channel, the Einstein coefficient for spontaneous emission becomes the measured decay rate ($A_{21} = \frac{1}{\tau}$). For what concern the line shape, it has not a simple form in general, so defining the effective linewidth:

$$I_{pk}\Delta\lambda_{eff} = \int_0^\infty I(\lambda) d\lambda \tag{4.6}$$

the line shape function can be written:

$$g(\nu) = \frac{I_{pk}}{\int I d\nu} = \frac{\lambda^2}{c} \frac{1}{\Delta\lambda_{eff}} \tag{4.7}$$

and the Fucthbauer-Landberg equation:

$$\sigma_{21} = \frac{\lambda^4}{8\pi\mu^2 c} \frac{1}{\tau\Delta\lambda_{eff}} \tag{4.8}$$

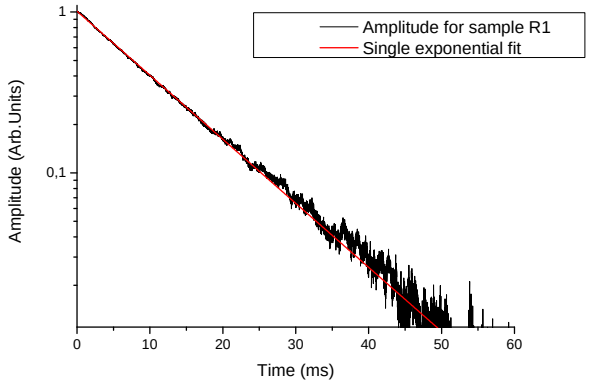

Figure 27: PL decay of Er photo-emission at $1.54\mu m$ fitted with single exponential curve.

From the spectrum reported in figure **??** it is possible to calculate the effective line-width, which results of $56nm$ and considering the radiative lifetime of $14.2ms$ reported in literature [6], the cross section is obtained, with a value of $1.24 \cdot 10^{-21} cm^2$ in good agreement with the values reported in literature [6, 26–28].

5 Interaction between Erbium and interfaces

The long lifetime associated with the transition ${}^4I_{13/2} \rightarrow {}^4 I_{15/2}$ of Er ions in silica limits the possibility of obtaining photonic and optoelectronic devices, because the long permanence of the ion in the excited state promotes non-radiative decay processes such as energy migration, cooperative up-conversion and concentration quenching.

It's known that the change in local photonic density of state (LDOS) may influence the decay rate of an emitter [5] and putting an interface at a distance d close to an emitter ($d < \lambda$) is the simplest way to influence the local photonic density of states [39–43]. In this section the case of Er^{3+} ions in silica interacting with thin films is explored, and in particular the possible coupling between emitted radiation and SPPs at $1.54\mu m$.

5.1 Theoretical model

The decay rate ($\Gamma_{i,j}$) of a spontaneous emission process between excited state i and ground state j, as photo-luminescence, is given by the *Fermi's golden rule* [44]:

$$\Gamma_{i,j} = \frac{2\pi}{\hbar}|M_{i,j}|^2\rho_j \tag{5.1}$$

where $M_{i,j}$ is the matrix element of the transition, linked to the wave-functions of the energy levels and ρ_j is the density of states of the optical field at the transition frequency (LDOS). The presence of an interface in proximity of an emitter can modify both the LDOS and the matrix element, but the second will be modified only if the overlap between the wavefunctions of an ion and an atom in the film is significant i.e., if atoms are nearest neighbours. Spontaneous emission is a typical quantum mechanical process where LDOS are seen substantially as vacuum fluctuations, but the classical point of view, in which density of states is seen as the ability of the surrounding structures to support emission, is equivalent and provide the same quantitative results [45, 46].

In the classical point of view, the emitter is considered as a forced dipole oscillator and the influence of the surface is taken into account by determining the total EM field acting on the dipole, including the dipole back-reflected field from the surface. The distance between the emitter and the surface is a fundamental parameter for the control of the lifetime, because the amplitude and phase of the reflected field determine if the emission is enhanced or suppressed. Besides, for a complete description of the phenomenon energy loss via transfer to the interface (coupling with SPPs) is to be considered. The analytical solution to this problem is given by Chance, Prock and Silbey (*CPS model*) [47, 48]. Considering the emitter as a forced damped dipole oscillator, the equation of motion becomes:

$$\frac{d^2\mu}{dt^2} + \gamma_0\frac{d\mu}{dt} + \omega^2\mu = \frac{e^2}{m}E_R \tag{5.2}$$

where μ is the dipole momentum, ω is the oscillator frequency without damping, m the effective mass, E_R the reflected field at dipole position and γ_0 the damping constant in the absence of the reflecting surface. The dipole momentum and the reflected field oscillate with the same (complex) frequency:

$$\mu = \mu_0 e^{-i[\omega+\Delta\omega]t} e^{\frac{-\gamma t}{2}} \tag{5.3}$$

$$E_R = E_0 e^{-i[\omega+\Delta\omega]t} e^{\frac{-\gamma t}{2}} \tag{5.4}$$

where $\Delta\omega$ and γ are the frequency shift and the decay rate in the presence of an interface. Using (5.3) and (5.4) and neglecting terms which contain γ^2 or $(e^2/\mu_0 m)E_0$, that are very small compared to ω^2 [49], eq. (5.2) yields:

$$\Delta\omega = \frac{\gamma^2}{8\omega} + \left[\frac{e^2}{2\mu_0 m\omega}\right]\mathbf{Re}(E_0) \tag{5.5}$$

$$\gamma = \gamma_0 + \left[\frac{e^2}{2\mu_0 m\omega}\right]\mathbf{Im}(E_0) \tag{5.6}$$

The frequency shift is quite small [48]. Equation (5.6) shows that the change of the decay rate of an emitter close to an interface is dictated by the out-of-phase component of the reflected field. Now what is to do is the calculation of the reflected electric field at the dipole position [50]. Once obtained it the decay rate for any dipole orientation can be derived combining perpendicular (γ_t) and parallel (γ_p) dipole components with respect to the interface:

$$\gamma_t^r = \gamma_0^r\left\{1 - \frac{3}{2}\mathbf{Im}\left[\int_0^\infty R_p \frac{u^3}{a_1} exp(-4\pi n_1 a_1 z/\lambda)du\right]\right\} \tag{5.7}$$

$$\gamma_p^r = \gamma_0^r\left\{1 + \frac{3}{4}\mathbf{Im}\left[\int_0^\infty \left[(1-u^2)R_p + R_t\right]\frac{u}{a_1} exp(-4\pi n_1 a_1 z/\lambda)du\right]\right\} \tag{5.8}$$

where u is the component of the wave-vector (of the dipole field) in the plane interface, normalized with respect to the far-field wave-vector k_1 of the dipole radiation field in medium 1 surrounding the emitter ($u = k_x/k_1$), n_1 is the refractive index, z the distance between the emitter and the interface, λ the emitting wavelength. The parameter $a_1 = -i\sqrt{1-u^2}$ is related to the perpendicular component of the wave-vector at the interface, while R_p and R_t are the Fresnel coefficients for p- and s-polarized light at the interface:

$$R_t = \frac{a_1 - a_2}{a_1 + a_2}, \quad R_p = \frac{\epsilon_1 a_2 - \epsilon_2 a_1}{\epsilon_1 a_2 + \epsilon_2 a_1} \tag{5.9}$$

with ϵ_1 the dielectric function of the medium embedding the emitter, ϵ_2 the complex one of the material beyond the interface and $a_2 = -i\sqrt{\frac{\epsilon_2}{\epsilon_1} - u^2}$.

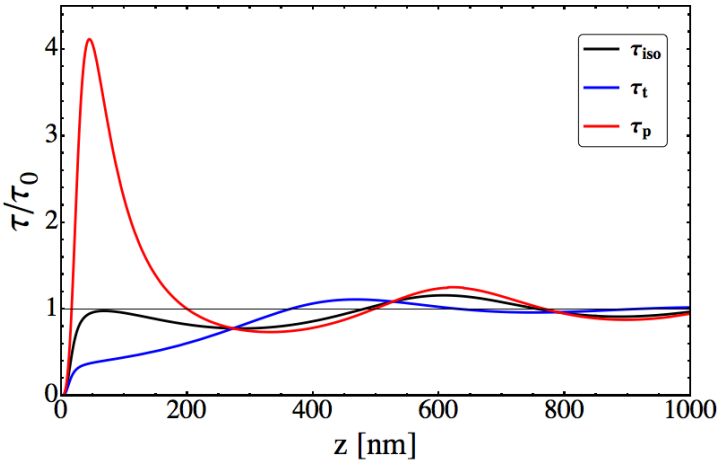

Figure 28: Variation of normalized lifetime as function of the distance (z) from a Au overlayer ($\epsilon_2 = -105.66 + i3.85$) for an Er-like emitter ($\lambda_{em} = 1540nm$) embedded in silica. Parallel, perpendicular and isotropic orientations are obtained from eq. (5.10), (5.7) and (5.8).

The normalized vector can range over all positive values so the reflection coefficients have to be evaluated for both real and complex angles of incidence, that correspond to incident waves propagating and evanescent respectively. If the dipoles have isotropic orientations with respect to the interface, the decay rate becomes:

$$\gamma_{iso} = \frac{1}{\tau} = \frac{2}{3}\gamma_p + \frac{1}{3}\gamma_t = \frac{2}{3}\frac{1}{\tau_p} + \frac{1}{3}\frac{1}{\tau_t} \tag{5.10}$$

5.2 Er^{3+} lifetime with CPS model

The aim of this section is the calculation of the Er^{3+} decay rate via the CPS model. The dipole momentum of Er^{3+} ions in silica have not a preferred orientation, so they are random also with respect to the interface and the decay rate takes the averaged form:

$$\gamma^r_{iso}(z) = \gamma^r_0 \left\{ 1 + \frac{1}{2}\mathbf{Im} \int_0^\infty \left[-R_p \frac{u^3}{a_1} + \Big((1-u^2)R_p + R_t \Big) \frac{u}{a_1} \right] exp(-4\pi n_1 a_1 z/\lambda) du \right\} \tag{5.11}$$

where γ^r_0 the radiative decay rate in the medium without interface.

Clearly the experimentally measured decay rate (γ_0) is to be considered as the sum of radiative (γ^r_0) and non-radiative (γ^{nr}_0) contributions, with the second being unchanged by the interface. In the following the decay rate will be indicated with γ when referred to the decay rate of a single dipole-like emitter,

and with Γ when referred to the integrated decay rate over a distribution of emitters. The Er-doped film has a finite thickness, so the Er distribution in the film is to be taken into account. Since atomic diffusion is negligible during the annealing [34], the concentration profile is assumed to be:

$$y = \begin{cases} f_0, \ z \in [z_0, z_0 + z_{Er}] \\ 0, \ z \notin [z_0, z_0 + z_{Er}] \end{cases} \tag{5.12}$$

where $z_0 = z_{min}$ is the distance of the $Er : SiO_2$ film from the interface, z_{Er} the thickness of the film and f_0 the constant value of Er concentration.

It's now possible to calculate the time dependence of the PL intensity:

$$I_{PL}(t) = I_0 \int_0^{\infty} f(z) \exp[\gamma^r_{iso}(z)t] dz = I_0 f_0 \int_{z_0}^{z_{Er}} \exp[\gamma^r_{iso}(z)t] dz \tag{5.13}$$

with γ^r_{iso} the decay rate for an emitter at a distance z from the interface and I_0 the stationary emission intensity. The dependence is not perfectly exponential, so the determination of the radiative decay rate ($\Gamma^r_{iso,calc}$) was performed fitting the first $20ms$ (where there was good agreement) of the normalized function, with a single exponential curve. If the non-radiative decay rate (Γ^{nr}_0) is kept constant the calculated Er lifetime becomes $\tau_{calc} = 1/(\Gamma_{iso,calc} + \Gamma^{nr}_0)$.

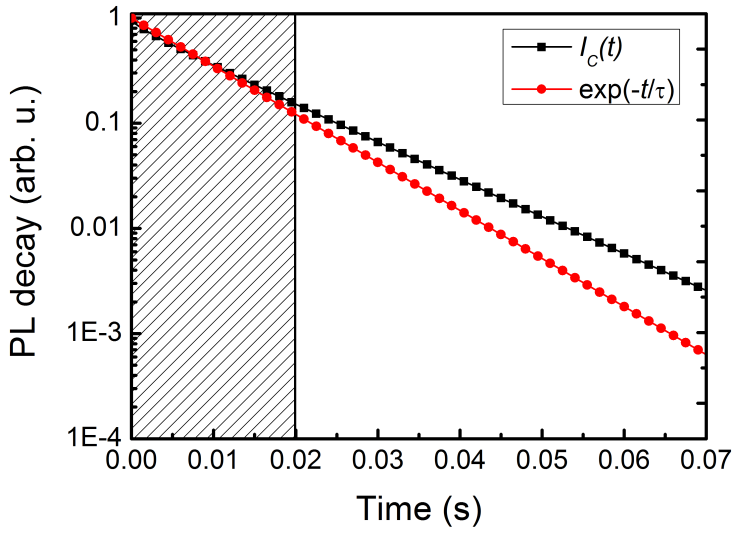

Figure 29: Comparison between time dependence of the PL intensity calculated with CPS model and a single exponential.

5.3 Radiative and non-radiative lifetime

For the determination of the two components, radiative and non-radiative, of the lifetime it is necessary an experimental measurements of the total lifetime. The

presence of the dielectric medium, with purely real component of the dielectric function, does not influence the radiative lifetime of an emitter in close proximity of a dielectric-dielectric interface, since dissipative contribution is linked to the complex part of the dielectric function. At low Er concentration, the decay rate (Γ_0) of the ${}^4I_{13/2} \rightarrow^4 I_{15/2}$ transition in a relaxed SiO_2 lattice is $70s^{-1}$ ($\tau_0^r = 14.2ms$), mainly due to radiative emission ($\Gamma_0 = \Gamma_0^r$) [6]. With this value in (5.11) and the procedure described previously, the radiative decay (Γ_{calc}^r) can be obtained for the reference samples. The difference between the experimental value and the calculated one is the non-radiative decay rate Γ^{nr}.

The calculation of radiative efficiency (q) is done from the calculated and experimental decay rates:

$$q = \frac{\Gamma^r}{\Gamma^r + \Gamma^{nr}} = \frac{\Gamma_{iso,calc}^r}{\Gamma_{exp}} \tag{5.14}$$

5.4 Metallic overlayer

The lifetime modification for the transition at $1540nm$ has been studied first for a gold film, which is a noble, plasmonic metal [34]. The study of this configuration is extremely useful both to study the influence of a dissipative medium in the process of photo-emission (see section 2.5) and to test the accuracy of numerical simulations used in susequent NHA analysis. In fact there is not yet a satisfactory analytical model developed to describe the NHA interaction with an emitter, due to the complexity of the NHA structure. Finite Element Simulations (FEM) have been carried out to try to understand the behaviour of the NHA interacting with an Er-like emitter, assuming every ion to be an emitting dipole (see section 3.3). These simulations have been replicated for a gold thin film, for which exists the analytical solution from the CPS model and the results have been compared, as shown in fig. 30.

The FEM results are in perfect agreement with the previsions of the CPS model, so they have been used to obtain a simulation of the NHA behaviour.

5.5 Power dissipation

In this section the different ways in which the decay can occur for an excited Er^{3+} in proximity of an interface are analysed. In a geometry with an infinitely extended plane above the emitter and another below it, if the energy flux through these two planes is calculated it is possible to obtain a rigorous separation between the energy flowing away by far-field ($F_\uparrow$) and energy transferred to the interface ($F_\downarrow$). The flux is calculated integrating the normal component of the complex Pointing vector (S^*) over the plane [48].

Dividing then the energy flux by the total energy radiated by the dipole, the probabilities of the two mechanism ($\gamma_\uparrow, \gamma_\downarrow$) are given by:

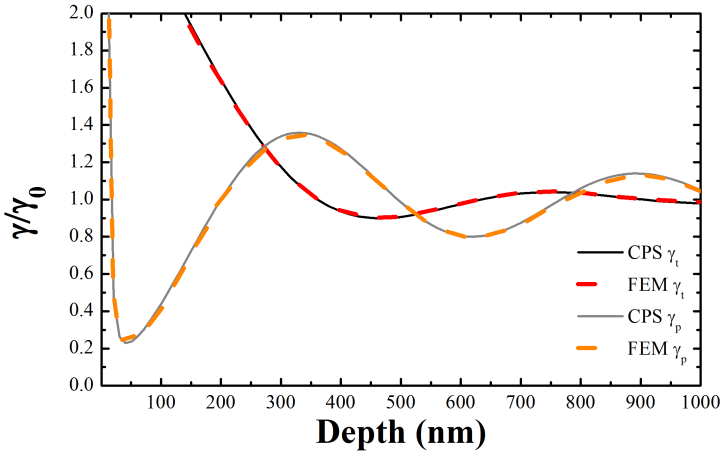

Figure 30: Comparison between simulation (FEM) and the CPS model for the variation of the normalized decay rate of an Er-like emitter ($\lambda_{em} = 1540nm$) as a function of the distance from a gold film [34].

$$\gamma_{\uparrow} = \Gamma_0^r \left\{ 1 + \frac{1}{2}\mathbf{Im} \int_0^1 \left[-R_p \frac{u^3}{a_1} + \Big((1-u^2)R_p + R_t \Big) \frac{u}{a_1} \right] \exp(-4\pi n_1 a_1 z/\lambda) du \right\} \tag{5.15}$$

$$\gamma_{\uparrow} = \Gamma_0^r \left\{ \frac{1}{2}\mathbf{Im} \int_1^{\infty} \left[-R_p \frac{u^3}{a_1} + \Big((1-u^2)R_p + R_t \Big) \frac{u}{a_1} \right] \exp(-4\pi n_1 a_1 z/\lambda) du \right\} \tag{5.16}$$

And:

$$\gamma_{\uparrow}(z) + \gamma_{\downarrow}(z) = \gamma_{iso}^r(z) \tag{5.17}$$

As a first approximation, $\gamma_{\uparrow}$ may be seen as radiative decay rate (γ^r) and $\gamma_{\downarrow}$ as non-radiative one (γ_{nr}). Now the far-field radiative efficiency (q_f) is computable: it represents the energy of photons which couples directly to far-field radiation, divided by the total energy emitted by the dipole. The far-field efficiency is thus given by:

$$q_f = \frac{\gamma^r(z)}{\gamma^(z) + \gamma^{nr}(z)} = \frac{\gamma_{\uparrow}(z)}{\gamma_{\uparrow}(z) + \gamma_{\downarrow}(z)} \tag{5.18}$$

Clearly q_f is not the effective radiative efficiency of the emitter, because of the presence of the contribution of surface plasmon polaritons which are considered as non-radiative decay channels, since they are expected to dissipate energy in the plane below the emitter. Actually SPPs are EM propagating modes on

the metal-dielectric interface that can couple out into far-field radiation or re-excite an Er ion close to the interface, thus contributing to the total emitted radiation [51].

To have a better understanding on how the energy leaves an excited dipole, it's important considering with more accuracy the behaviour of the near-field, which extends at most at a distance λ_{em} from the emitter. The near field emitted from a dipole contains components with a large range of wave-vectors k, but only if $k < k_1$ it will propagate directly into the far-field (k_1 is the far-field wave-vector in the matrix containing the dipole). Near to a planar surface, a large wide range of k_x (the wave-vector in the plane of the interface) exist too, the emitted radiation can couple to modes having in-plane momenta greater than k_1, like SPPs in case of metal films, modes not accessible to incident waves.

The power dissipation of a dipole in the presence of a metal interface can be written as a sum of three different contributions [52]:

$$P = Pphoton + P_{SPP} + P_{LSW} \tag{5.19}$$

where P_{photon} is the power radiated via photons, P_{SPP} via surface plasmons and P_{LSW} via the so called *lossy surface waves*. If the emitters are randomly oriented, at a certain distance from the interface, the power dissipation spectrum can be obtained from the imaginary part of the integrand in (5.11) as a function of the normalized wave-vector [45].

At small distances ($z < \lambda/50$) the non-radiative contribution due to the coupling with LSW is dominant. Going farther from the interface the LSW contribution decreases rapidly and becomes negligible. SPPs coupling vanishes with the distance but remains detectable to a range comparable to the λ_{em}.

To calculate the contribution of the SPP modes to the total decay rate, integration of the peak above the light line as function of u, has been performed. After this, also the non-radiative contribution has been calculated:

$$\gamma_{LSW} = \gamma_{nr} - \gamma_{SPP} \tag{5.20}$$

and thus the near-field radiative efficiency:

$$q_F^*(z) = \frac{\gamma_r + \gamma_{SPP}}{\gamma_r + \gamma_{SPP} + \gamma_{LSW}} \tag{5.21}$$

In an ideal case in which all the energy associated to the surface plasmons can be coupled-out, γ_{SPP} can be considered an actual radiative decay channel also in the far-field.

If the depth of the Er-doped layer is accounted, Γ_r, Γ_{SPP} and Γ_{LSW} can be evaluated.

6 Control of Erbium emission lifetime by interaction with Nanohole arrays

Studying the variation of the $Er3+$ decay rate at $1540nm$, it has been found that the Er radiative emission can couple with SPP modes on the noble metal-silica interface. This coupling can significantly shorten the lifetime reducing the permanence of the ion in te excited state and thus the probability of non-radiative recombinations. The possible interesting development is to induce an efficient coupling-out of the SPP into the far-field. This aim could be reached using plasmonic nano-structures, which thanks to the electromagnetic field confinement and near-field enhancement, can in principle enhance the luminescent properties of emitters placed in close proximity. A lot of works had been carried out on the interaction between an emitter and a plasmonic nano-particle, showing how the enhancement of the luminescence is function of the distance from the nano-particle [53]. For what concern the nanohole array-emitter interaction not many works are present in literature [54–59], but their peculiar feature of extraordinary transmission (EOT), joint to the possibility of coupling out the SPPs propagating on the NHA surface, without using gratings.

6.1 Interaction between Er and NHA

The presence of a nanostructure in proximity to Er ions can in principle both enhance or quench the characteristic emission at $1540nm$. When plasmonic nano-particles are close to an emitter, two competitive mechanisms take place: near-field enhancement and reduction of the quantum efficiency due to energy transfer to the nano-structure. For NHAs, no theoretical description of the phenomenon has been developed, and their optical properties in presence of active species has still to be investigated.

6.1.1 Sample synthesis

The synthesis of the samples uses the techniques presented in the previous sections. The aim of the work is to study the interaction between Erbium and nanohole arrays placed at different distances, and to compare the results with numerical simulations. To do this the idea is to deposit an $Er : SiO^2$ layer via magnetron sputtering on silica glass substrate, to cover it with a silica spacer increasing the thickness on each sample and fabricate the gold NHA over the spacer.

Two samples have been used as test samples for Er-deposition and subsequent treatments:

Er:SiO^2 deposition The deposition of the Er-doped layer was performed via magnetron co-sputtering, using an RF source fixed at $250W$ for the silica ad a DC source at $3W$ for Erbium, this permits to obtain a concentration of Er of 1.0%. During the sample deposition the holder was rotating to have a good homogeneity of the film composition and thickness and the atmosphere was a

Sample	$Er:SiO_2$ layer (nm)	Silica over-layer (nm)
S_1	30	200
R_1	30	0

Table 6: Features of the test samples for PL measurements. Sample S_1 presents a $100nm$ NHA below the Er-doped layer, besides sample R_1 is as test reference sample.

mixture of $5\%O_2$ and $95\%Ar$ at pressure of $5 \cdot 10^{-3}mbar$. Magnetron sputtering allows to control the distances between Er-doped layer and the surface of the sample, just depositing un-doped silica during the same process. The choice was to fabricate two sets of four samples with four different distances between a $20nm$ thick Er-doped layer and the NHA, before the Er-doped layer, a $30nm$ thick silica layer was deposited. The thickness was then measured using a profilometer and the results are reported below:

Sample	Spacer [nm]	Thickness measured [nm]	Thickness expected [nm]
M_{30}	30	80 ± 5	80
M_{60}	60	113 ± 5	110
M_{90}	90	140 ± 5	140
M_{120}	120	160 ± 5	170
N_{30}	30	83 ± 5	80
N_{60}	60	115 ± 5	110
N_{90}	90	141 ± 5	140
N_{120}	120	175 ± 5	170

For the first set of M samples the choice was to perform the thermal annealing after the Er deposition and before the NHA fabrication, to avoid eventual modifications on the NHA structure due to the high temperature, for the set N the annealing was done after the deposition, but covering the NHA with a silica layer to prevent damages due to the annealing process.

For each thickness and each set two samples were prepared, one reference sample labelled, in the following, with M^{ref} or N^{ref} and one with the NHA, labelled with M or N.

Nanohole fabrication After the Er-doped deposition, the NHA synthesis was performed using NSL for depositing PS mask, as described in section 2, RIE process for the reduction and magnetron sputtering for gold deposition. A $22'$ RIE was carried out on the M series of samples and a $24'$ one for the N series, because the RIE had been less effective and the erosion of the PS particles was not as efficient as for the test samples S_1 and S_2. The conditions of the RIE process have been the same used for the test RIE, $9 \cdot 10^{-3}mbar$ pressure, $12W$ power and the atmosphere was a mixture of $27\%Ar$ and $73\%O_2$. After the

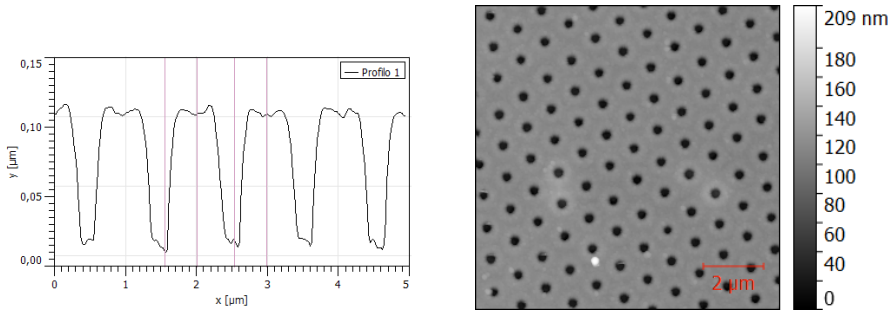

(a) AFM profile

(b) AFM image

Figure 31: AFM image and profile of the NHA after a $200nm$ silica deposition on test sample S_1. Is clear that the silica overlayer does not influence the deep of the holes, since it is of $\sim 100nm$ before and after the deposition.

RIE process the gold deposition was executed with the magnetron sputtering, obtaining a $\sim 100nm$ layer. After this the mask have been removed via ultrasound sonication in toluene, and after this a $\sim 150nm$ of silica deposition was carried out to protect the NHA from the high temperature of the annealing.

Thermal annealing As pointed out before a thermal annealing is necessary to activate the Pl emission of Er ions in the silica matrix. This process restores the defects in the matrix and avoids the loss of energy absorbed from the Er due to non-radiative modes. Moreover, high temperatures could modify the properties of the gold NHA, in particular the can induce a blue-shift of the EOT peak, modifying the holes' lattice.

Two ways can be followed to reduce this modifications: annealing the samples before the NHA synthesis or cover the NHA with a SiO_2 over-layer and perform the annealing after the metal deposition. The first has the advantage that the NHA does not suffers the high temperature treatment, but the disadvantage that the activation is carried out before the various processes necessary for the NHA synthesis, thus more time passes between activation and PL measurements and also they undergo the action of many solvents and acid substances, which can somehow influence the quality of the emission. The second way has the disadvantage that the NHA must suffer the high temperature and could be modified by this, but the activation is performed as the last process before the PL measurement. For the set M the first way was followed, for the set N the second.

Before the treatment a series of incremental annealing were performed on the test sample S_1, with the nanohole array covered with a $200nm$ silica layer, to evaluate the eventual blue-shift caused by the temperature. The annealing were carried out in N_2 atmosphere from 300° to 900°, with increment of 100° for 1 hour treatment at each temperature.

As it's clear from figure 32 there is an appreciable blue-shift of the peak pass-

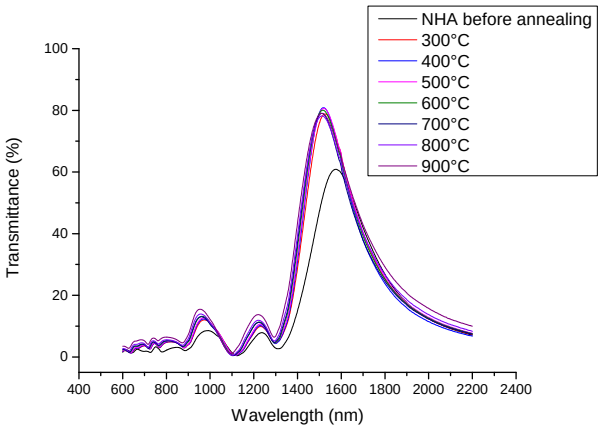

Figure 32: Transmission spectra of S_1, after a series of thermal annealing at increasing temperatures. The annealings were performed in N_2 atmosphere.

ing from environmental temperature to 300°, but the peak remains substantially in the same position after the treatment at the higher temperatures.

6.2 Characterization and measurements

Transmittance spectra To have a control on the matching between the EOT peak of the NHA and the emission peak of Erbium, optical transmittance measurements have been performed. The transmittance spectra were measured at normal incidence with respect to the NHA plane, while the rare earth emission in a glassy matrix is in general angularly isotropic, therefore it is difficult to estimate *a priori* the matching of the EOT peak with Er^{3+} emission wavelength. So to avoid a possible mismatch between the two peaks, the choice has been to have a slightly larger resonance peak for EOT, with respect to the one on test sample R_1. This could be done by making NHAs with greater holes radius.

PL measurements The characterization of the Er^{3+} luminescent emission properties of the samples and the interaction mechanisms between the Er ions and NHAs proceeds through the measurements of photo-luminescence (PL) (both integrated and time-resolved) at room temperature using resonant ($\lambda = 488nm$) Er excitation condition. A CW Ar laser was used as the excitation source using the experimental set-up described in section 1.3.

Under resonant excitation no difference in the PL peak position or shape were detected.

It's interesting to note that the PL signal can be detected from both sides pf the samples and this feature could be interesting for possible photonic application, since the NHA can act as a filter, selecting only the wavelengths matching the EOT peaks.

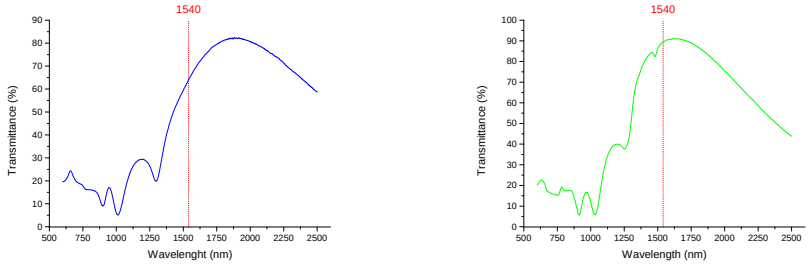

(a) Transmittance spectrum of sample M_{90}. Holes' diameter of $\sim 750nm$.

(b) Transmittance spectrum of sample N_{90}. Holes' diameter of $\sim 600nm$.

Figure 33: Transmittance spectra for samples M_{90} and N_{90}. It's reported the position of the Er emission peak.

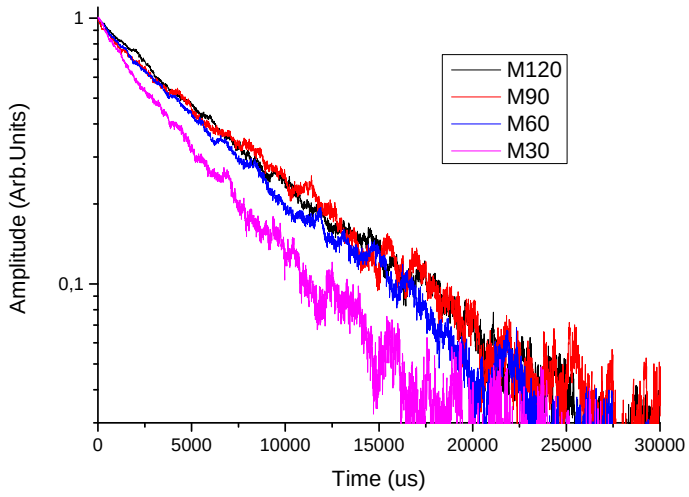

Figure 34: Photo-emission decay for sample series *M*. It's clear the lifetime reduction as the distance between Er-doped layer and NHA decreases.

6.3 Finite Element Method simulations

Since a theoretical model that predicts the variation of the emission properties of an emitter in the proximity to a NHA has been not yet be developed yet, it was necessary to use finite element method (FEM) simulations to predict the lifetime variations and thus to obtain more informations about the near-field of the emitter. FEM simulations were performed with the commercial software COMSOL Multiphysics [60].

Finite element methods [61] take into account a finite space domain, discretizes it in small cells and solve the equations on every node of the mesh. These methods can work either in the frequency domain (finite difference frequency domain - FDFD) or in the time domain (FDTD). In the FDFD the Helmoltz (1.35) equation is solved, with standard boundary conditions. The condition of finite domain is necessary to keep the equation system sufficiently small to be manageable, but creates problems due to back-scattering of waves by the outer surface. The proper scattering boundary condition must then be imposed at the outer boundary, to permit the numerical analogous of the outgoing waves [62]. The method transforms the problem in a linear system of matrix, with a Helmholtz equation for each node, and solves this system with a linear solver.

For the simulation of the emitters one dipole at a time have been considered. The signal from an arbitrary distribution of dipoles and their variations of decay rates were then recovered by integrating the results from differently placed dipoles. In this case the use of periodic boundary conditions, using for the simulation of periodically ordered structures, was not suitable. Indeed, in fact, a mirrored dipole would be generated in each cell, with the result that the simulation would describe a system where dipoles have the same periodicity of the nano-structure, which is not the case. The alternative is to extend the simulation domain to include several unitary cells together, using Perfectly Matched Layer (PML - an additional (artificial) domain that absorbs the incident radiation without producing reflections) at the boundaries to suppress backscattering. For the correct implementation of the model, the minimum size of the domain has to be the one that ensures that near-field from the dipole emission vanishes before reaching the boundaries.

Homogeneous film As a first step, the effect of a semi-infinite film have been modelled to determine the domain minimum size and to validate the method using as a benchmark the electrodynamical derivation of the CPS model proposed by Chance et al.[47] and discussed in section 2.4. A simulation domain surrounded by a sphere of radius ($R \sim 3\lambda_{em}$) was found to be enough for the correct modelling of the emitter lifetime variation in close proximity of an interface, as it will be shown in the following. To simulate an Er-like emitter ($\lambda_{em} = 1540nm$) interacting with the film, the domain have been divided into two hemispheres, one representing the silica matrix, the other representing the film. The interface has been placed at the z=0 plane. Dipoles have been placed so that their projection on the interface plane falls in the centre of the simu-

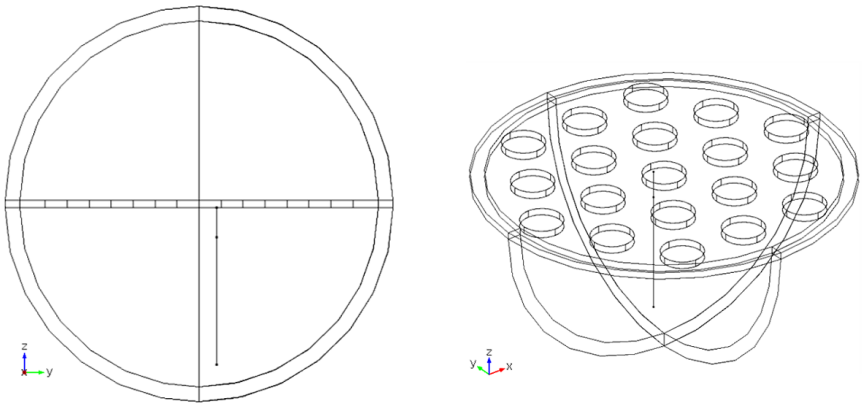

(a) Side-view (b) Perspective view

Figure 35: Wireframe views of the NHA-emitter interction model.

lated sphere ($x = 0, y = 0$). The z coordinate of the dipoles (i.e., the distance from the interface) has been varied from 1 nm to 1000 nm. For each z position, the decay rate for a dipole with parallel (γ_p) and perpendicular (γ_t) orientation with respect to the interface was calculated. The normalized decay rate was evaluated by integrating the Poynting vector ($\mathbf{S}$) on a closed surface (Σ) encircling the dipole (and not any part with absorbitive material) and dividing by the decay rate (γ_0^r calculated without the interface:

$$\frac{\gamma^r}{\gamma_0^r} = \frac{\int_\Sigma \mathbf{S} d\sigma}{\int_\Sigma \mathbf{S}_0 d\sigma} \tag{6.1}$$

In figure 30 there is a comparison between γ_t and γ_p both calculated with FEM simulation and analytic electrodynamic model (CPS), and the numerical calculations result in good agreement with the analytical prevision. To take into account the Er distribution in the z direction typical for the Er:SiO2 co-sputtered films, the procedure described in section 2.4 has been used, leading as expected to the same calculated lifetime values.

Nanohole array The simulations of the emitter-NHA interaction have been carried out in an analogous way. In this case, the whole simulated domain is constituted by silica, except for the NHA film extending in the XY plane, and centred at z=0, as shown by Fig. 35. Unlike the film geometry, the translational invariance in the XY plane doesnt hold any more and it has to be replaced with the periodic Honeycomb lattice resulting from the NSL process.

As already discussed, the periodic boundary conditions can not be used for the correct evaluation of the decay variation due to the replication of the emitter. Thus, 19 XY unit cells have been modelled, in order to obtain the domain size determined for the film geometry. Because the periodicity of the lattice, the

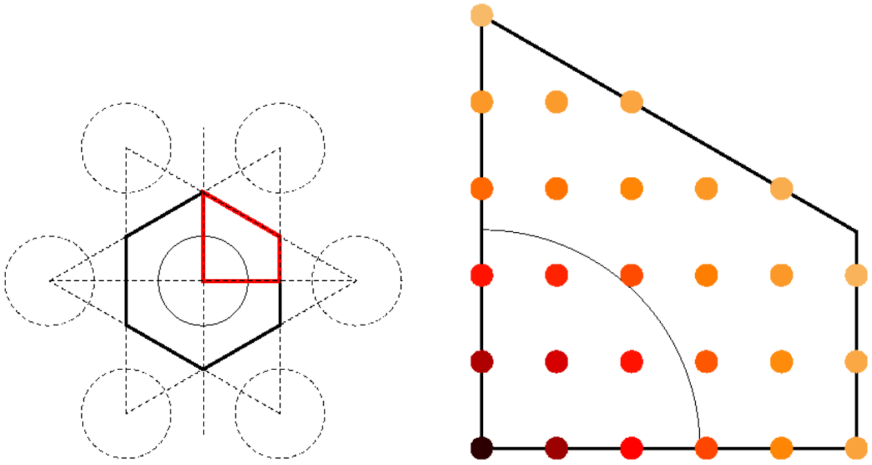

(a) Construction of the Wigner-Seitz cell. Dashed lines are simmetry planes; black line encircles the WS cell; red line encircles the sampled cell exploiting lattice simmetries and $\hat{x}$ and $\hat{y}$ simmetries.

(b) Sampling points in the minimal cell:27 points. Poins on the edges and vertces have coefficient $c_{ij} <$ in averages.

Figure 36: Wigner-Seitz cell: construction and sampling points.

behaviour of the emitter can be sampled in one unitary cell only. Moreover, due to the symmetries in $\hat{x}$ and $\hat{y}$ direction, the hexagonal unit cell can be reduced to only a quarter, as shown by Fig. 36.

Once the minimum cell has been defined, for each z value a grid with 27 points representing the dipole position in the XY plane have been defined according to Fig.36, to sample as accurately as possible the whole cell. Moreover, for each position in the XY plane 3 different dipole orientation have to be taken into account, since in addition to the perpendicular orientation, the parallel one has to considered along $\hat{x}$ and $\hat{y}$ the axes of the NHA. Thus, when the emitters have an isotropic orientation configuration the decay rate becomes $\gamma_{iso} = 1/3(\gamma_t + \gamma_{pz} + \gamma_{pz})$.

Fig.37 shows the decay rate (γ^{iso}) for the 27 positions of an Er-like emitter as a function of the distance from a NHA with lattice parameter $a_0 = 1030nm$; the black line represents the dipole at the center of the hole. The colors are as lighter as the projected distance ($r = \sqrt{x^2 + y^2}$) from the center of the hole increases and the variation of the decay rate becomes more prominent for small distances from the NHA. As a comparison, the blue curve represents the result obtained in the Au film case. Furthermore, it is worth noting that in the range $0 < z < \lambda_{em}/2$ there are two regions at $z \sim 200nm$ and $z \sim 600nm$ where the modification of the lifetime is almost insensitive to the position of the emitter in the XY plane.

To average dipole emission in this case, the equation (5.13) must be rewritten considering the differences given by the XY position of the emitter. The integral

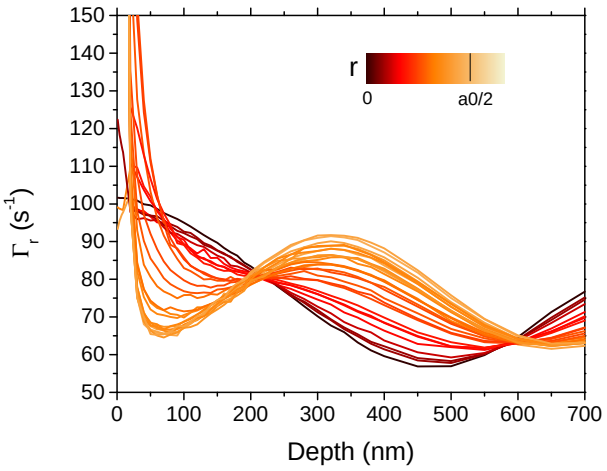

Figure 37: Simulated $\gamma_r(z)$ for emitter placed at different positions in the XY plane for a $a_0 = 1030nm$ NHA. The color map indicates the distance from the centre of a hole in the WS cell, as in fig. 36(b).

is still present in the $\hat{z}$ direction, while in the XY plane, the integration is substituted by a sum over the 27 emitter positions sampled in the minimum cell and denoted by the couple of i and j indices:

$$I_{PL}(t) = I_0 A \sum_{i,j} c_{ij} \int_0^{+\infty} f(x_i, y_i, z) e^{-\gamma_{iso}(x_i,y_i,z)t} dz \tag{6.2}$$

where the coefficients c_{ij} account for the normalization of the points shared by adjacent cells and $A = \frac{1}{\sum_{i,j} c_{ij}}$ is a global normalization factor.

6.4 Experimental results and discussion

The goal of this work was to evaluate if the interaction between a $Er : SiO_2$ film and a gold plasmonic nanohole array can induce a variation in the photo-emission efficiency of excited Erbium ions, and how this variation is correlated to the distance between the Er-doped layer and the NHA.

In order to obtain the emission efficiency:

$$q = \frac{\Gamma_r}{\Gamma_r + \Gamma_{nr}} \tag{6.3}$$

the total decay rate $\Gamma_{exp} = \Gamma_r + \Gamma_{nr}$ is needed.

For each sample of the set M and N the Er^{3+} lifetime was extracted from the PL measurements. The hypothesis was that the photo-luminescence decay could be fitted by a single exponential curve $I_{PL}(t) = Ae^{t/\tau} + y_0$, thus the

experimental lifetime τ_{exp} can be obtained and the total decay rate $\Gamma_{exp} = \frac{1}{\tau_{exp}}$ calculated. This procedure was performed for the reference samples and for the NHA samples. Measurements are listed in table below:

(a) Reference samples measurements

Sample	τ_{exp}^{ref} [ms]
M_{30}^{ref}	11.4 ± 0.6
M_{60}^{ref}	11.8 ± 0.6
M_{90}^{ref}	12.4 ± 0.6
M_{120}^{ref}	10.2 ± 0.5
N_{30}^{ref}	10.3 ± 0.5
N_{60}^{ref}	9.4 ± 0.5
N_{90}^{ref}	8.8 ± 0.4
N_{120}^{ref}	10.3 ± 0.5

(b) NHA samples measurements

Sample	τ_{exp}^{ref} [ms]
M_{30}	4.9 ± 0.2
M_{60}	6.7 ± 0.3
M_{90}	7.7 ± 0.4
M_{120}	7.2 ± 0.4
N_{30}	6.5 ± 0.3
N_{60}	6.9 ± 0.4
N_{90}	7.6 ± 0.4
N_{120}	8.7 ± 0.4

Table 7: Measured lifetime for the two sets of samples M and N.

For the lifetime measurements a 5% error was estimated from repeated measurements. Errors of the derived quantities were than propagate with the formulas reported on [63].

From the measured decay rates (Γ_{exp}^{ref}) of the reference samples is now possible to calculate the non-radiative decay rate Γ_{nr}, making use of the radiative decay rate expected from the CPS model calculation (Γ_{CPS}):

$$\Gamma_{nr} = \Gamma_{exp}^{ref} - \Gamma_{CPS} \tag{6.4}$$

Γ_{CPS} was computed using the commercial software *Mathematica 10.1*, assuming a $20nm$ thick layer of $Er : SiO_2$ with an uniform concentration of Er ions, placed at the same distances used for the experimental samples, from an Air-silica interface, which is the case of the reference samples. Results are presented in table **??**.

Once obtained the non-radiative decay rate, with the reasonable hypothesis that the presence of the metallic over-layer or the NHA does not modify the intrinsic non-radiative decay rate, it is possible to give an estimation of the radiative decay rate (Γ_r) in presence of the nanohole array subtracting the non-radiative one (Γ_{nr} from the experimental decay rate measured for the NHA (Γ_{exp}^{NHA}):

$$\Gamma_r = \Gamma_{exp}^{NHA} - \Gamma_{nr} \tag{6.5}$$

The calculated radiative decay rates are reported in table 9 and are than compared with the FEM simulation in figures 39 and 38.

Sample	Γ_{exp}^{ref} $[1/s]$	Γ_{CPS} $[1/s]$	Γ_{nr}
M_{30}^{ref}	88 ± 4	55.4	32 ± 4
M_{60}^{ref}	85 ± 4	58.1	27 ± 4
M_{90}^{ref}	81 ± 4	60.3	20 ± 4
M_{120}^{ref}	98 ± 5	62.1	36 ± 5
N_{30}^{ref}	97 ± 5	55.4	42 ± 5
N_{60}^{ref}	106 ± 5	58.1	48 ± 5
N_{90}^{ref}	114 ± 6	60.3	53 ± 6
N_{120}^{ref}	97 ± 5	62.1	31 ± 5

Table 8: Experimental, CPS radiative and calculated non-radiative decay rates.

Sample	τ_{exp}^{NHA} [ms]	Γ_{exp}^{NHA} $[1/s]$	Γ_r $[1/s]$
M_{30}	4.9 ± 0.2	204 ± 9	172 ± 10
M_{60}	6.7 ± 0.3	149 ± 7	123 ± 9
M_{90}	7.7 ± 0.4	129 ± 7	110 ± 8
M_{120}	7.2 ± 0.4	139 ± 7	103 ± 9
N_{30}	6.5 ± 0.3	154 ± 8	112 ± 9
N_{60}	6.9 ± 0.4	145 ± 7	97 ± 9
N_{90}	7.6 ± 0.4	132 ± 7	78 ± 9
N_{120}	8.7 ± 0.4	115 ± 6	84 ± 8

Table 9: Experimental lifetimes and decay rates, and computed radiative decay rates.

As it's clear from figure 38 the samples of N series is in agreement within the errors with numerical simulations. From this fact it's possible to observe that the second way used to fabricate the samples, allows a better reconstruction of silica matrix defects around Erbium ions, which produces a reduction of the total decay rate. The figure shows a decrease of the radiative decay rate as the distance from the interface increases, this is due to a progressive weaker coupling between dipole emission and SPP modes, as distance increases.

The agreement with FEM calculations permits to obtain two interesting indications. On one side it is an indication that the single dipole approximation, made applying the FEM procedure is a good way to simulate the interaction between a population of emitters and an interface or a nano-structure. This result is of primary importance since it shows that a random oriented distribution of dipole-like emitters can be studied simply considering one dipole at time and performing an incoherent sum over the whole distribution. Experimentally this is true if each dipole is substantially independent from the others, and this happens if the Er concentration is not too high.

The second result is that Finite Element Method simulations are a good

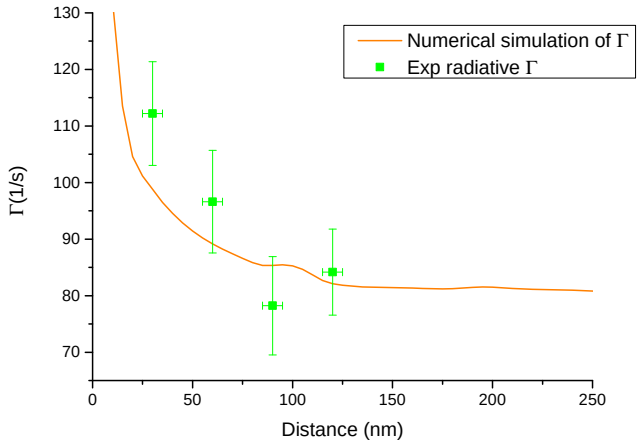

Figure 38: Comparison between FEM simulation of radiative decay rate and experimental radiative decay rate for set *N*.

way of modeling the behaviour of the electromagnetic field and can be used to study various systems, in particular the cases in which there is a lack of effective analytical models, as in case of NHAs.

For what concern the *M* of samples, as it can be seen in figure 39 the trend followed by the experimental points is in quite good agreement with the simulated curve, but the measured decay rate are higher than the expected ones. This is due to a higher non-radiative component of the decay rate. This could be caused by different factors like a less efficient action of the annealing process, which fixed the matrix defects worse than in the case of *N* series, or because of a major occurrence of the concentration the quenching phenomenon caused by not optimal configuration of the environment around the Er ions.

In conclusion is possible to calculate the efficiency of the photo-emission for Er ions in presence of the nanohole array at the interface and for the reference samples, results in table 10.

As it can be seen, for each sample there is an improvement of the efficiency of the emission for the Er-ions, this confirms the role of plasmonic nanohole array in helping the emission process, by coupling in the near-field the radiation emitted with the SPP modes, and with the subsequent re-emission into the far-field thanks to the grating properties of the lattice of holes.

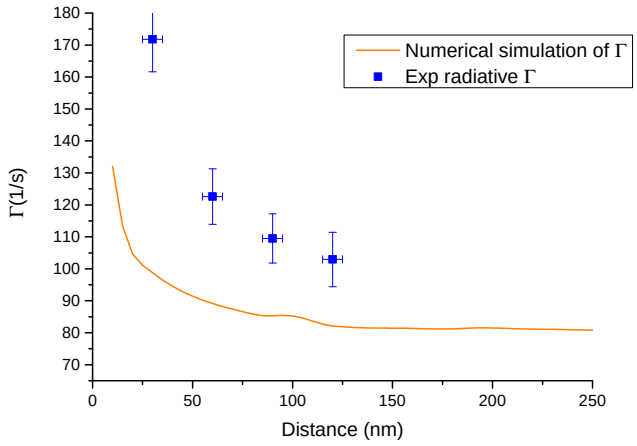

Figure 39: Comparison between FEM simulation of radiative decay rate and experimental radiative decay rate for set *M*.

Sample	q^{ref}	q^{NHA}
M_{30}	0.63	0.84
M_{60}	0.69	0.82
M_{90}	0.75	0.84
M_{120}	0.63	0.74
N_{30}	0.57	0.73
N_{60}	0.55	0.67
N_{90}	0.53	0.59
N_{120}	0.68	0.73

Table 10: Photo-emission efficiency for reference samples and for NHA.

7 Conclusions

In this work the properties of plasmonic nanohole arrays have been studied, the presence of the extraordinary optical transmission resonance has been verified and the dependence of its position on the lattice parameter has been pointed out. The dependence of the peak shape and position on holes' diameter has also been studied, finding that by increasing the nanohole diameter the peak undergoes a red-shift and strong broadening.

Nanosphere litography has been presented and optimize as a versatile and cost-effective method for producing nanostructures, making use of single-layer masks of polystyrene nanospheres. In particular used in combination with reactive ion etching processes (RIE) it resulted useful in producing ordered structures like arrays of nanoholes and obtaining a fine tuning of the diameter of the holes, without varying the lattice parameter.

In the present work, nanohole arrays have been applied to the study of the modification of the decay rate of an emitter in proximity to an interface. Erbium was chosen as the emitter because of its great importance in the field of optical communication. The variation of the Er lifetime has been verified in the presence of nanohole arrays, which brings to an enhancement of the photoluminescent emission, thanks to the strong coupling in the near-field between dipolar emission of Er ions and SPP Bloch waves on the interface between the nanohole array and the silica matrix in which the ions are embedded.

The trend of variation of the decay rate with the distance between the Er-doped layer and the nanohole array is in good agreement with the results of Finite Element Simulations carried out to supply the lack of analytical models for the description of these systems. The agreement between simulations and experimental results is a validations of the approximation used in the numerical simulation, in which the solution for the problem of interaction is found considering each ion singularly and then performing an incoherent sum over the whole distribution. This approximation could be used in general to study a lot of of systems in which there is the presence of dipole-like emitters randomly distributed.

The study carried out in this thesis work presents many possible future developments. In particular optimizing the matching between the EOT peak and the Er emission wavelength and examining in depth the variation of photoluminescence intensity and lifetime changing the angle of incidence or the polarization of the exciting light, could lead to a deeper understanding of the mechanisms of interaction between nanostructures and emitters, and to an optimized control of their properties.

References

[1] R. P. Feynman. There's plenty of room at the bottom. *Engineering and Science*, 23:22–36, 1960.

[2] N. Taniguchi et al. On the basic concept of nanotechnology. *Proceedings of the International Conference on Production Engineering, Part II*, pages 18–23, 1974.

[3] S. A. Maier. *Plasmonics: fundamental and application.* Springer, 2007.

[4] T. W. Ebbesen, H. J. Lezec, H. F. Ghaemi, T. Thio, and P. A. Wolff. Extraordinary optical transmission through sub-wavelength hole arrays. *Nature*, 391:667–669, 1998.

[5] E. M. Purcell. Spontaneous emission probabilities at radio frequencies. *Phys. Rev.*, 69(681), 1946.

[6] A. Polman. Erbium implanted thin film photonic materials. *Journal of Applied Physics*, 82:1–39, 1997.

[7] P.B. Johnson and R.W. Christy. Optical constants of the noble metals. *Phys. Rev. B*, 6(12):4370–4379, 1972.

[8] Alexander Vial, Anne-Sophie Grimault, Demetrio Macias, Dominique Barchiesi, and Marc Lamy de la Chapelle. Improved analytical fit of gold dispersion: Application to the modeling of extinction spectra with a finite-difference time-domain method. *Phys. Rev. B*, 71(085416), 2005.

[9] F. Hao and P. Nordlander. Efficient dielectric function for fdtd simulation of the optical properties of silver and gold nanoparticles. *Chem. Phys. Lett.*, 446:115–118, 2007.

[10] Gustav Mie. Beitrage zur optik truber medien, speziell kolloidaler metallosungen. *Ann. Phys.*, 330(3):377–445, 1908.

[11] H. A. Bethe. Theory of diffraction by small holes. *Phys. Rev.*, 66(7:8), 2007.

[12] A. Roberts. Electromagnetic theory of diffraction by a circular aperture in a thick, perfectly conducting screen. *J. Opt. Soc. Am. A*, 4(10):19701983, 1987.

[13] A. Degiron, H.J. Lezec, and T.W. Ebbesen N. Yamamoto. Optical transmission properties of a single subwavelength aperture in a real metal. *Optical Communication*, 239:61–66, 2004.

[14] C. Genet and T. W. Ebbesen. Light in tiny holes. *Nature*, 445:39–46, 2007.

[15] I. R. Hooper and J. R. Sambles. Dispersion of surface plasmon polaritons on short-pitch metal gratings. *Phys. Rev. B*, 65(165432), 2002.

[16] Shih-Hui Chang, Stephen Gray, and George Schatz. Surface plasmon generation and light transmission by isolated nanoholes and arrays of nanoholes in thin metal films. *Opt. Express*, 13(8):3150–3165, 2005.

[17] H. F. Ghaemi, Tineke Thio, D. E. Grupp, T. W. Ebbesen, and H. J. Lezec. Surface plasmons enhance optical transmission through subwavelength holes. *Phys. Rev. B*, 58(11):6779–6782, 1998.

[18] T. Thio, H. F. Ghaemi, H. J. Lezec, P. A. Wolff, and T. W. Ebbesen. Surface-plasmon-enhanced trasmission through hole arrays in cr films. *J. Opt. Soc. Am. B*, 16(10), 1999.

[19] A. Degiron and T. W. Ebbesen. The role of localized surface plasmon modes in the enhanced transmission of periodic subwavelength apertures. *J. Optics A: Pure and Applied Optics*, 7(2), 2005.

[20] Christy L. Haynes and Richard P. Van Duyne. Nanosphere lithography: A versatile nanofabrication tool for studies of size-dependent nanoparticle optics. *J. Phys. Chem. B*, 105(24), 2001.

[21] Frank Burmeister, Claudia Schaffle, Thomas Matthes, Johannes Boneberg Matthias Bohmisch, and Paul Leiderer. Colloid monolayers as versatile lithographic masks. *Langmuir*, 13:2983–2987, 1997.

[22] Liang Li, Tianyou Zhai, Haibo Zeng, Xiaosheng Fang, Yoshio Bando, and Dmitri Golberg. Polystyrene sphere-assisted one-dimensional nanostructure arrays: synthesis and applications. *J. Mat. Chem.*, 21(40), 2011.

[23] N. D. Denkov, O. D. Velev, P. A. Kralchevsky, I. B. Ivanov, H. Yoshimura, and K. Nagayama. Two-dimensional crystallization. *Nature*, 361, 1993.

[24] S. M. Rossnagel, J. J. Cuomo, and W. D. Westwood. *Handbook of plasma processing technology.* Noyes Publications, 1990.

[25] D. M. Mattox. *Handbook of physical vapor deposition (PVD) processing.* William Andrew Elsevier Science distributor, Norwich, N.Y. Oxford, 2010.

[26] W. J. Miniscalco. Erbium-doped glasses for fiber amplifiers at 1500 nm. *J. Lightwave Technol.*, 9:234–250, 1991.

[27] A. M. Glass. Fiber optics. *Physics Today*, 46(34), 1993.

[28] E. Desurvire. The golden age of optical fiber amplifiers. *Physicis Today*, 47(20), 1994.

[29] S. Hufner. *Optical spectra of the transparent rare earth compounds.* Academic Press, 1978.

[30] C. Layne, W. Lowdermilk, and M. J. Weber. Multiphonon relaxation of rare-earth ions in oxide glasses. *Phys. Rev. B*, 16(10), 1977.

[31] P. M. Becker, A.A. Olsson, and J. R. Simpson. *Erbium-doped fiber amplifiers: fundamental and technology.* Academic Press, 1999.

[32] A. Kenyon. Recent developments in rare-earth doped materials for optoelectronics. *Progr. Quant. Electron.*, 26(225), 2002.

[33] E. Cattaruzza, G. Battaglin, F. Visentin, and E. Trave. Er-doped films by rf magnetron co-sputtering. *J. Non-Crystalline Solids*, 355:1128–1131, 2009.

[34] B. Kalinic, T. Cesca, N. Michieli, C. Scian, G. Battaglin, P. Mazzoldi, and G. Mattei. Controlling the emission rate of ions by dielectric coupling with thin films. *J. Phys. Chem. C*, 2015.

[35] A. Polman. Erbium as a probe of everything? *Physica B: Condensed Matter*, 300:78–90, 2001.

[36] T. Forster. Zwischenmolekulare energiewanderung und fluoreszenz. *Ann. Phys.*, page 55, 1948.

[37] E. Snoeks, P. Kik, and A. Polman. Recent developments in rare-earth doped materials fo optoeleptronics. *Prog. Quant. Electron.*, 26(225), 2002.

[38] W. L. Barnes, E. J. Tarbox R. I. Laming, and P. Morkel. Absorption and emission cross section of er doped silica fibers. *Quantum electronics, IEEE J. of*, 27:1004–1010, 1991.

[39] K. Drexhage, M. Fleck, H. Kuhn, F. Schafer, and W. Sperling. Beeinflussung der fluoreszenz eines europium-chelates durch einen spiegel. *Ber. Bunsenges. Phys. Chem.*, 70(1179), 1966.

[40] K. H. Drexhage, H. Kuhn, and F. P. Schfer. Variation of the fluorescence decay time of a molecule in front of a mirror. *Berichte der Bunsengesellschaft fr physikalische Chemie*, 72:329, 1986.

[41] K. H. Drexhage. Monomolecular layers and light. *Scientific American*, 222:108–119, 1970.

[42] K. Drexhage. Influence of a dielectric interface on fluorescence decay time. *Journal of Luminescence*, 1-2:693–701, 1970.

[43] K. H. Drexhage. Interaction of light with monomolecular dye layers. *Elsevier*, pages 163–232, 1974.

[44] E. Fermi. Quantum theory of radiation. *Reviews of modern physics*, 4:87–132, 1932.

[45] W. Barnes. Fluorescence near interfaces: the role of photonic mode density. *Journal of modern optics*, 45:661–699, 1998.

[46] M. Yeung and T. Gustafson. Spontaneous emission near an absorbing dielectric surface. *Phys. Rev. A*, 54(5227), 1986.

[47] R. Chance, A. Miller, A. Prock, and R. Silbey. Fluorescence and energy transfer near interfaces: The complete and quantitative description of the eu/mirror systems. *The Journal of Chemical Physics*, 63(1589), 1975.

[48] R. Chance, A. Prock, and R. Silbey. Molecular fluorescence and energy transfer near interfaces. *Adv. Chem. Phys*, 37(65), 1978.

[49] R. Chance, A. Prock, and R. Silbey. Comments on the classical theory of energy transfer. *The Journal of Chemical Physics*, 62(2245), 1975.

[50] K. G. Sullivan and D. G. Hall. Enhancement and inhibition of electromagnetic radiation in plane-layered media. i.plane-wave spectrum approach to modeling classical effects. *J. Opt. Soc. Am. B*, 14:1149–1159, 1997.

[51] P. Andrew and W. L. Barnes. Molecular fluorescence above metallic gratings. *Phys. Rev. B*, 64(125405), 2001.

[52] G. Ford and W. Weber. Electromagnetic interactions of molecules with metal surfaces. *Physics Reports*, 113:195–287, 1984.

[53] P. Anger, P. Bharadwaj, and L. Novotny. Enhancement and quenching of singlemolecule fluorescence. *Physical review letters*, 96(113002), 2006.

[54] M. Saboktakin, X. Ye, U. K. Chettiar, N. Engheta, C. B. Murray, and C. R. Kagan. Plasmonic enhancement of nanophosphor upconversion luminescence in au nanohole arrays. *ACS nano*, 7:7186–7192, 2013.

[55] Y. Mochizuki, M. Fujii, S. Hayashi, T. Tsuruoka, and K. Akamatsu. Enhancement of photoluminescence from silicon nanocrystals by metal nanostructures made by nanosphere lithography. *Journal of Applied Physics*, 106(013517), 2009.

[56] A. G. Brolo, S. C. Kwok, M. G. Moffitt, R. Gordon, J. Riordon, and K. L. Kavanagh. Enhanced fluorescence from arrays of nanoholes in a gold film. *Journal of the American Chemical Society*, pages 14936–14941, 2005.

[57] A. G. Brolo, S. C. Kwok, M. D. Cooper, M. G. Moffitt, C.-W. Wang, R. Gordon, J. Riordon, and K. L. Kavanagh. Surface plasmon-quantum dot coupling from arrays of nanoholes. *The Journal of Physical Chemistry B*, 110:8307–8313, 2006.

[58] E. Verhagen, L. Kuipers, and A. Polman. Field enhancement in metallic subwavelength aperture arrays probedby erbium upconversion luminescence. *Opt. Express*, 17:14586–14598, 2009.

[59] R. J. Moerland, L. Eguiluz, and M. Kaivola. Shaping single emitter emission with metallic hole arrays: strong focusing of dipolar radiation. *Opt. Express*, 21:4578–4590, 2013.

[60] C. Multiphysics and C. M. H. T. Module,. *Comsol multiphysics users guide*, comsol multiphysics 3 edition, 2010.

[61] M. Morgan and K. Mei. Finite-element computation of scattering by inhomogeneous penetrable bodies of revolution. *IEEE Transactions on Antennas and Propagation*, 27(2):202–214, 1979.

[62] R. Mittra and O. Ramahi. Absorbing boundary conditions for the direct solution of partial differential equations arising in electromagnetic scattering problems. *Finite Element and Finite Difference Methods in Electromagnetic Scattering*, 2, 1990.

[63] M. Loreti. *Teoria degli errori e fondamenti di statistica*. Ed. Privata, 2006.

List of Figures

List of Tables